

An image-computable spatio-chromatic receptive  
field model of the midget retinal ganglion mosaic  
across the retina

Nicolas P. Cottaris<sup>1\*</sup>, Brian A. Wandell<sup>2</sup> and David H. Brainard<sup>1</sup>

<sup>1</sup>Department of Psychology, University of Pennsylvania, Philadelphia,  
PA, USA.

<sup>2</sup>Department of Psychology, Stanford University, Stanford, CA, USA.

\*Corresponding author(s). E-mail(s): [cottaris@upenn.edu](mailto:cottaris@upenn.edu);  
Contributing authors: [wandell@stanford.edu](mailto:wandell@stanford.edu); [brainard@upenn.edu](mailto:brainard@upenn.edu);

### Abstract

Image-computable models of retinal ganglion cell (RGC) mosaics that are synthesized and constrained jointly by optical, anatomical and physiological properties, and which operate on images defined by their spatial-spectral radiance, do not currently exist. Here, we deploy a novel computational framework which synthesizes mosaics of linear spatio-chromatic receptive fields (RFs) of ON midget RGCs (mRGCs) by integrating published anatomical, physiological, and optical quality measurements, all varying with eccentricity. We use the synthesized mRGC mosaics to simulate both *in vivo* and *in vitro* physiological experiments and demonstrate the model's consistency with published data. The model enables computation of how visual performance is shaped by the representation of visual information provided by the linear spatiochromatic processing stage of midget RGCs. The developed computational framework carefully accounts for the effect of physiological optics on mRGC responses, enables comparison of *in vivo* and *in vitro* data, and allows exploration of how different assumptions about RF organization, such as selectivity for the type of cones pooled by the RF center mechanism, affect physiological responses and psychophysical performance. The open-source and freely available implementation provides a platform for understanding how the linear spatiochromatic receptive field representation of the mRGCs shapes visual performance, as well as a foundation for future work that incorporates response nonlinearities, temporal filtering, and extends to additional RGC mosaics.

**Keywords:** retinal ganglion cells, receptive field, model

047 **1 Introduction**

048  
049 An important aim in computational visual neuroscience is to create accurate computer  
050 simulations of how neurons in the visual pathways encode and respond to visual scenes.  
051 These simulations, often called digital twins, are a quantitative description of the  
052 visual system. They enable links between the neural representation and perception  
053 and provide a tool for evaluating the effects of blinding disease and its treatment.

054 Over the last ten years we have built an open-source software platform, ISETBio  
055 (Image Systems Engineering Tools for Biology) [1], which serves as a digital twin for  
056 the initial stages of the human visual system. Previously, we described how ISETBio  
057 models (a) the formation of the retinal image, (b) the excitation of the cone pho-  
058 toreceptors, (c) phototransduction, and (d) fixational eye movements [2–4]. We and  
059 others have employed ISETBio to model human vision, including sensitivity to spa-  
060 tial contrast [2, 3], the impact of chromatic aberration on acuity [5], the encoding of  
061 information from natural images captured by cones [6], the effects of optics and cone  
062 density across the visual field on performance [7], and the influence of initial visual sig-  
063 nals on tasks like judging surface properties and lighting [8, 9]. We also used ISETBio  
064 to help interpret experimental measurements of retinal ganglion cells [10].

065 Here, we describe an extension of ISETBio to model the mosaic of a class of retinal  
066 ganglion cells (RGCs), the midget RGC (mRGC) mosaic. RGCs are the only pathway  
067 for information transmission from the retina to the brain, and their properties surely  
068 impact visual performance on many tasks. The spike trains transmitted via the axons  
069 of one million RGCs that form the human optic nerve, represent the signals from  
070 roughly 6.5 million cones and 110 million rods [11, 12]. Of these RGCs, mRGCs are  
071 a particularly important subtype, comprising 80% of the perifoveal RGCs and 45%  
072 of the peripheral RGCs. In the very central fovea, it has been estimated that the  
073 mRGCs are 95% of the RGC population [13].

074 The role of the mRGCs in limiting spatial and color vision is still debated [14].  
075 Simulation of performance using image computable models of the mRGC mosaic offers  
076 a powerful tool for understanding the visual information encoded by these cells, espe-  
077 cially because they are very hard to measure and isolate experimentally. We have four  
078 primary goals for this human retina model.

079 First, the model must distinguish the contributions of the eye’s optics and pho-  
080 toreceptors from the subsequent post-receptoral retinal circuitry. This separation is  
081 crucial for incorporating key physiological measurements, some of which are made *in*  
082 *vitro* without the eye’s optics. Failing to isolate the optical effects would prevent us  
083 from using this vital collection of data.

084 Second, the model must capture responses across a large portion of central  
085 retina. This is important because we and others are interested in how the retinal  
086 representation shapes performance not just in the fovea but also for peripheral viewing.

087 Third, the model must integrate diverse data types, including optical, anatomical,  
088 and physiological measurements. A comprehensive formulation is necessary because  
089 retinal ganglion cell (RGC) responses are shaped by all three of these factors.

090 Fourth, we aim for an extensible framework. The current implementation uses a  
091 linear spatiochromatic receptive field, which serves as a good initial approximation.  
092

The framework is designed to incorporate future extensions—such as response non-linearities, temporal dynamics, and additional RGC classes—to improve the model’s accuracy over time. The following points describe how our implementation achieves these goals.	093
1. <i>Separating representations.</i> Our mRGC model operates on the cone mosaic signals. This design isolates the post-receptoral circuitry (cone-to-mRGC), which is the pathway measured in <i>in vitro</i> experiments where the eye’s optics are removed [15, 16]. This separation is also valuable for interpreting experiments that use adaptive optics to eliminate optical blur [10]. While the components are separable, our implementation integrates the optics, cone sampling, and mRGC circuitry into a complete, image-computable pipeline. This full pathway allows us to simulate the transformation of a visual stimulus into an mRGC response, matching the conditions of <i>in vivo</i> measurements [17–19] and enabling predictions of human performance under natural viewing conditions.	094
2. <i>Representation across the visual field.</i> Visual performance varies across the visual field, and a key contribution of our model is that it allows computation of the mRGC representation continuously across the retina from the fovea out to 30°, along any meridian. Achieving this goal required implementation of novel algorithms for synthesizing mRGC RF mosaics.	095
3. <i>Multiple data types.</i> By explicitly representing different biological stages, our model enables algorithms that combine anatomical, physiological, and optical data. Incorporation of multiple types of measurements from the literature is critical because at present no one type of data sufficiently constrains mRGC properties across the visual field.	096
4. <i>Extensible.</i> The current implementation is a linear spatial pooling model, a useful approximation for stimuli with modest contrast. The software’s modular design provides a foundation for future extensions. We can incorporate known nonlinear properties that shape mRGC responses, including phototransduction effects [20]; spatial and static nonlinearities, which often differ between ON and OFF pathways [21–24]; temporal dynamics [25]; and response noise [26]. Furthermore, the mRGC model is a suitable base for developing models of other types of RGCs, such as parasol and bistratified cells [27].	097
1.1 Model overview	098
Fig. 1 provides a model overview. Computation begins with the image spectral radiance, such as produced by a calibrated monitor. A model of the human optics (including chromatic aberrations) and spectral filtering by the lens is used to compute the retinal irradiance. Retinal irradiance is spectrally filtered by the macular pigment and then spatially and spectrally sampled by the cone photoreceptor mosaic. The parameters of the optics, macular pigment and cone mosaic all vary across the visual field, according to measurements in the literature [2].	099
The mRGC mosaic extension is composed of spatial receptive fields (RFs) whose center and surround responses are weighted sums of signals from the cone mosaic.	100
	101
	102
	103
	104
	105
	106
	107
	108
	109
	110
	111
	112
	113
	114
	115
	116
	117
	118
	119
	120
	121
	122
	123
	124
	125
	126
	127
	128
	129
	130
	131
	132
	133
	134
	135
	136
	137
	138

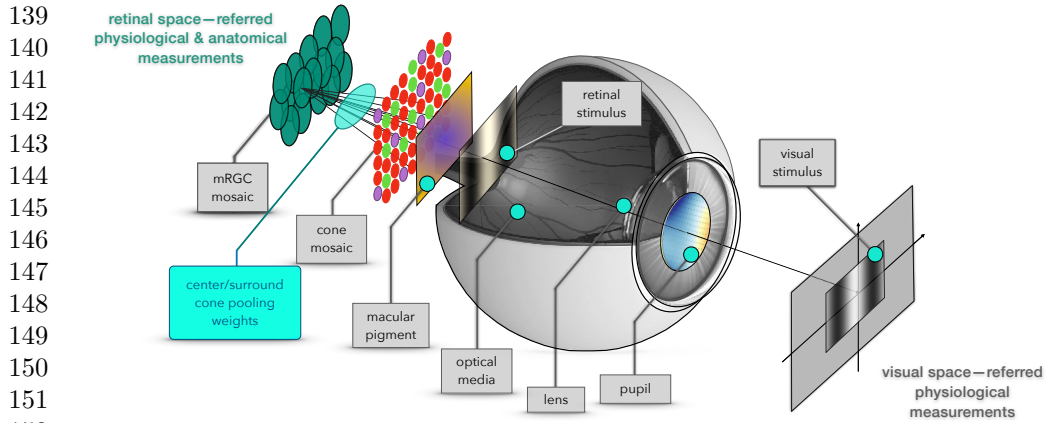


**Fig. 1 Model overview.** The extant ISETBio model computes the mosaic of cone excitations. The model mRGCs are obtained by connecting their RFs to the cone mosaic. The connectivity matrix is constrained by anatomy and optimized through forward simulation of physiological measurements, so that the synthetic mRGCs are consistent with optical, anatomical and physiological data across the visual field.

The wiring between the input cone mosaic and the mRGC mosaic is initially determined based on anatomical constraints, such as cone and mRGC densities, and is subsequently refined using optimization algorithms that align the model's spatial RF properties with physiological measurements.

A key challenge is the scarcity of *in vitro* physiological data across the visual field which could be used to directly determine the wiring between the two mosaics. To address this, our algorithm primarily leverages more widely available *in vivo* data for the optimization, while validating the model against *in vitro* data where it exists. The resulting model is simultaneously consistent with cone light encoding, anatomical properties (including those of mRGCs and H1 horizontal cells), and both *in vitro* and *in vivo* physiological data. This makes the model versatile for simulating visual stimulation under *in vivo*, *in vitro*, and adaptive optics paradigms.

### 1.1.1 Relationship to previous computational models of RGCs

To our knowledge, no previous model of RGCs has attempted to realistically capture the effects of the front end encoding in the visual system, specifically the eccentricity and wavelength-varying nature of physiological optics, and the eccentricity-varying spatio-chromatic properties of the cone mosaic. Instead previous models of RGCs have either completely ignored the impact of physiological optics [28, 29], or employed very simplistic models of the eye's optics [30]. Moreover, previous RGC models were designed to either operate directly on visual space, completely ignoring the spatio-spectral filtering by the tri-chromatic cone mosaic [28], or have employed simplistic implementations of the cone mosaic [30]. Finally, none of the previous models are constructed to operate on stimuli defined in terms of their physical spatial-spectral radiance, as they are designed to operate on light intensity defined stimuli [28, 30]. As

such, previous models can not capture the rich spatio-chromatic interactions between stimuli and physiological optics, and how their combined effects shape RGC responses. Indeed, we have recently shown that spatio-chromatic interactions between stimuli and physiological optics can have profound effects of the response properties of midget ganglion cells [31].	185 186 187 188 189
On the other hand, previous computational models of RGCs have focused on other, also important, components of the RGC circuit, that our linear spatio-chromatic model does not currently address, such as processing by retinal interneurons [28–30, 32], temporal dynamics [28–30, 32], contrast grain control [28, 33], and spike generation [28, 29, 33]. We plan to extend our linear spatiochromatic model of mRGCs to include several of these components, as described in section 4.2.2.	190 191 192 193 194 195 196
<b>1.1.2 Paper organization</b>	197
The remainder of this paper is organized as follows.	198 199
• In section 2 we describe the model’s construction stages, including, how the mRGC receptive field lattice is generated from anatomical data (section 2.1), how cones get connected to the mRGC RF centers using anatomical and physiological constraints (section 2.2), and how cone connections to mRGC RF surrounds are derived by optimizing against <i>in vivo</i> data (section 2.3).	200 201 202 203 204
• In section 3 we present, validate, and discuss a first application of the model. Specifically, we illustrate examples of synthesized mRGC mosaics (section 3.1), confirm that the model mRGC spatial RFs are consistent with <i>in vivo</i> (section 3.2), and <i>in vitro</i> data (section 3.3), demonstrate the significant impact of physiological optics (section 3.4), and how simpler Difference-of-Gaussians models can fail to capture the true surround pooling (section 3.5), and finally we present first applications of the developed model, which illustrate how the model can be used to estimate the contribution of the mRGC mosaic to spatiochromatic contrast sensitivity across the visual field (section 3.6).	205 206 207 208 209 210 211 212 213
• In section 4, we summarize our work, discuss ongoing applications of the model in its current stage, and discuss the model’s present limitations and planned expansions.	214 215 216
<b>2 Methods</b>	217 218
The synthesis of mRGC RF mosaics occurs in three stages. In the first stage, we generate spatial lattices representing the RF centers of cells in the mRGC mosaic and the position of cones of the cone mosaic that provides input to the mRGC mosaic. In the second stage, we connect the input cone mosaic to the RF centers of the mRGC mosaic. In the third stage, we connect the input cone mosaic to the RF surrounds of the mRGC mosaic.	219 220 221 222 223 224 225 226 227 228 229 230

231 **2.1 Generating the spatial position lattice of mRGC RF  
232     centers (Stage 1)**

233 We begin by generating a lattice that represents the  $(x, y)$  positions of mRGC RF  
234 centers. This process comprises three sub-stages, components of which are illustrated  
235 in Fig. 2.

- 236 • **Stage 1A:** We estimate the mRGC RF center densities along the four principal  
237 meridians ( $0^\circ$ ,  $90^\circ$ ,  $180^\circ$ , and  $270^\circ$ ). These estimates are based on human data  
238 [34, 35]. We take the ON-mRGC density to be half of the total mRGC density,  
239 ignoring the possible density differences between ON- and OFF-center mRGCs.  
240 The meridian functions are depicted in Fig. 2A.
- 241 • **Stage 1B:** We generate a continuous, two-dimensional map representing the mRGC  
242 RF density map, depicted in Fig. 2B. This map is created by linearly interpolating  
243 the meridian estimates, and it serves as a target for the algorithm in the next stage.
- 244 • **Stage 1C:** We synthesize a sampling lattice that represents the  $(x, y)$  positions of  
245 the mRGC RF centers. The lattice is created using the iterative algorithm that we  
246 introduced earlier [2] for generating cone mosaics, replacing the two-dimensional  
247 cone density map with the target mRGC RF density map. A typical lattice of mRGC  
248 RF positions is obtained after about 1,300 iterations and has a density that varies  
249 smoothly over space, matching the target density, as illustrated in Fig. 2C. Example  
250 patches of mRGC RF center mosaics synthesized at eccentricities of  $0^\circ$  and  $20^\circ$   
251 along the temporal horizontal meridian, are depicted in Figs. 2D & 2E, respectively.
- 252

253 The same procedure is used to generate the lattice that represents the  $(x, y)$  posi-  
254 tions of cones, but, in this case, using the meridian densities of cone photoreceptors in  
255 human retina [36] as targets. The density of cones in the synthesized cone lattice also  
256 varies smoothly over space and matches closely the target cone density, as illustrated  
257 in Fig. 2F.

258 **2.2 Connecting cones to mRGC RF centers (Stage 2)**

259 The connections between cones and mRGC centers are constrained by (1) anatomical  
260 data across the retina, specifically, the ratio of densities of mRGC RF centers to cones  
261 [34], and (2) *in-vitro* physiological data from peripheral retina, that (a) indicate that,  
262 unlike OFF-center mRGCs, which draw indiscriminately from all three cone types  
263 [15, 37, 38], ON-center mRGCs draw only from L- and M-cones, and (b) quantify the  
264 degree of RF center overlap in neighboring mRGCs [39]. In the present version of the  
265 model, we only model ON-center mRGCs. The cone to mRGC RF center connectivity  
266 is established in 3 sub-stages, summarized here.

- 267 • **Stage 2A:** In the first substage, each L- and M-cone gets connected to a single  
268 mRGC RF center; single RF centers can receive input from more than one cone.  
269 At this substage, each connected cone has unit connection weight. S-cones are not  
270 connected because they do not contribute to ON-center mRGCs. This initial cone-  
271 to-RF center connectivity often results in inhomogeneities in the composition of  
272 neighboring mRGCs RF centers, which are dealt with in the next stage. Algorithmic  
273 details regarding this substage are provided in Supplemental Section A.1.

277  
 278  
 279  
 280  
 281  
 282  
 283  
 284  
 285  
 286  
 287  
 288  
 289  
 290  
 291  
 292  
 293  
 294  
 295  
 296  
 297  
 298  
 299  
 300  
 301  
 302  
 303  
 304  
 305  
 306  
 307  
 308  
 309  
 310  
 311  
 312  
 313  
 314  
 315  
 316  
 317  
 318  
 319  
 320  
 321  
 322

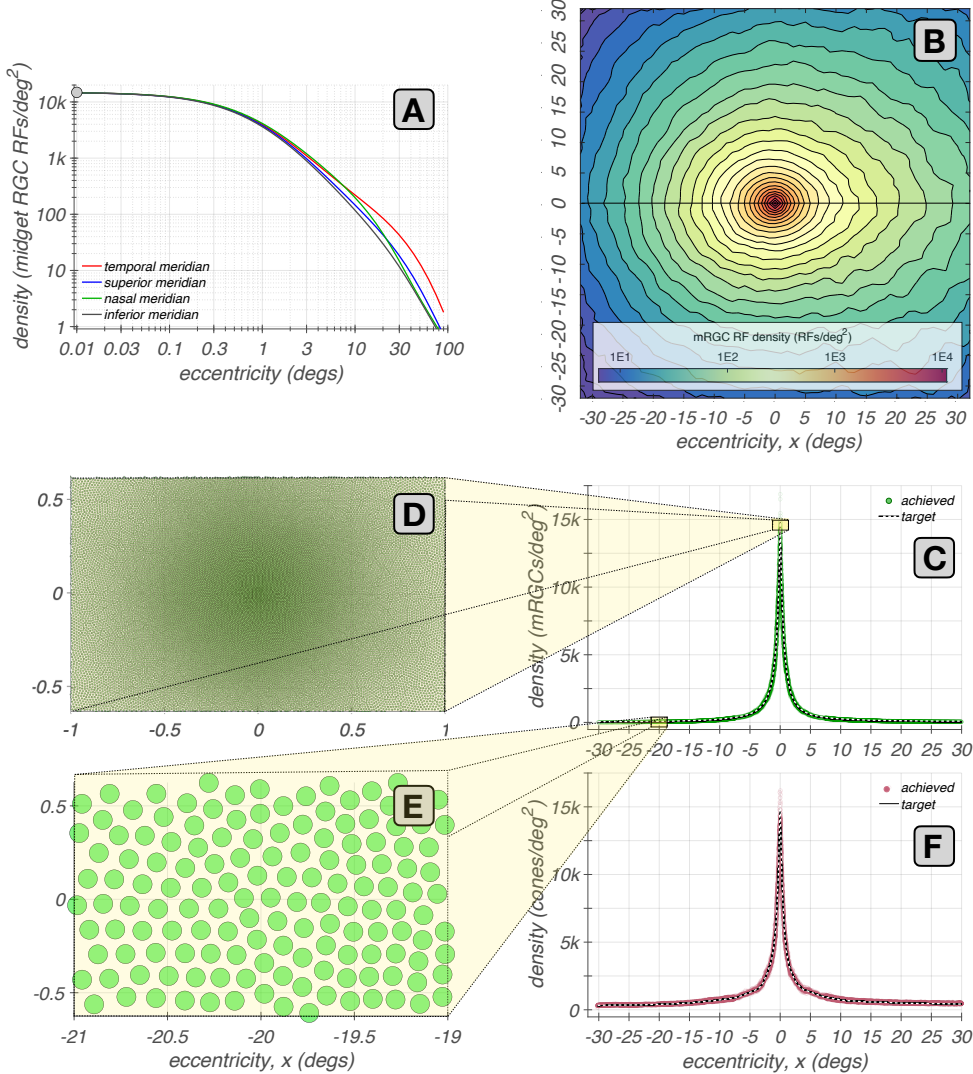


**Fig. 2 Eccentricity-varying mRGC RF position lattices.** **A:** Meridian density functions of mRGC RFs [34]. **B:** Two-dimensional mRGC RF density map obtained by interpolating the four meridian density functions. **C:** Achieved and target densities of mRGC RF centers along the horizontal meridian (green disks and white dashed line, respectively). **D & E:** Examples of  $2^\circ \times 1^\circ$  mosaics of mRGC RF centers at eccentricities of  $0^\circ$  and  $20^\circ$ , respectively, along the temporal meridian. **F:** Achieved and target densities of cones along the horizontal meridian (maroon disks and white dashed line, respectively).

- **Stage 2B:** This substage refines the center connections to establish a balance between the spectral purity and spatial compactness of the mRGC RF centers, which is quantified by a single parameter,  $\phi$ . For the body of this work, all mRGC

mosaics are generated by maximizing spatial compactness, but the option to maximize spectral purity allows testing of different scenarios where mRGC RF centers may be biased to some extent towards cone type selective pooling [15, 16]. At this substage, connected cones retain their unit connection weights. Algorithmic details regarding this substage are provided in Supplemental Section A.2.

- **Stage 2C:** Finally, the mutual exclusivity constraint enforced in substages 2A and 2B is lifted, and single cones are permitted to connect to multiple nearby mRGC RF centers. The extent of divergence varies with retinal eccentricity, being minimal in the fovea and increasing towards the periphery to match experimental observations [39]. This is done by varying the exponent of a supra-Gaussian distribution that describes the spatial weighting profile of cone connections to the RF centers which at this substage become non-binary. Algorithmic details regarding this substage are provided in Supplemental Section A.3.

We illustrate Stage 2 by examining key properties of synthesized mRGC RF center mosaics at each of the three substages.

### 2.2.1 Mosaics with convergent-only cone connections (stage 2A)

Example mosaics of RF centers synthesized at four eccentricities along the temporal horizontal meridian at the end of this substage are depicted in Fig. 3, where each green ellipse represents the spatial extent of the RF center of a single mRGC. At this stage, the pooling weight of each cone is set to unit.

For the foveal mosaic depicted in Fig. 3A, RF centers connect to just a single cone. Note how RF center sizes increase as we move towards parafoveal regions to the left and right sides of Fig. 3A. This is due to the continuously increasing, with eccentricity, cone aperture in the input cone mosaic. The empty regions in this foveal mRGC RF center mosaic correspond to the location of S-cones which are not pooled by the model.

In the parafoveal mosaic depicted in Fig. 3B, RF centers mostly receive inputs from two cones, whereas in the more peripheral mosaics depicted in Figs 3C & 3D, RF centers connect to multiple cones. Note that the number of cones connecting to RF centers does not correspond precisely to RF center size, because cone aperture and inter-cone spacing both increase with eccentricity. At all eccentricities, however, mRGC RF center mosaics tile the retinal space with no spatial overlap or voids, except at the sparse positions where S-cones are located.

### 2.2.2 Mosaics synthesized under different spatial compactness/spectral purity tradeoffs (stage 2B)

This substage allows for different optimizations of cone pooling within the mRGC RF centers, which is controlled by the spatial compactness/spectral purity tradeoff parameter,  $\phi$ . At this stage, the pooling weight of each cone is still set to unit, independent of the value of  $\phi$ .

Fig. 4 depicts examples of mRGC RF center mosaics all synthesized at a single eccentricity ( $12^\circ$  along the temporal meridian), but under different values of  $\phi$ . The mosaic synthesized under  $\phi = 1$ , where spatial compactness is maximal and spectral purity constraint is not enforced, is depicted in Fig. 4A. Note that the RF centers

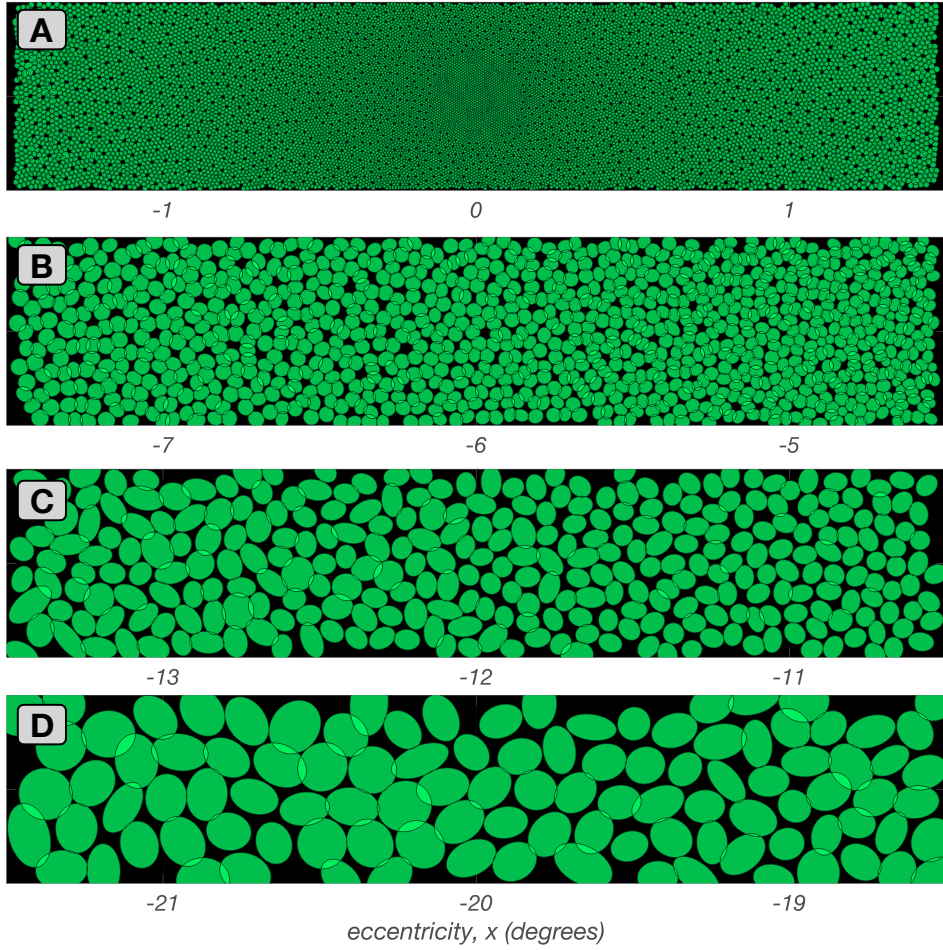


**Fig. 3 Stage 2A mRGC RF mosaics.** Each panel shows a  $3.0^\circ \times 0.5^\circ$  mosaic of synthesized mRGC RF centers at a different visual field location from fovea to periphery. The green ellipses depict a spatial region that encompasses all cones pooled by single RF centers. **A:** Foveal mosaic, in which RF centers receive signals from a single L- or M-cone. **B:** Mosaic centered at  $6.0^\circ$  along the temporal horizontal meridian, in which RF centers receive signals from 2–3 L/M-cones. **C:** Mosaic centered at  $12.0^\circ$  along the temporal horizontal meridian, in which RF centers receive signals from 3–4 L/M-cones. **D:** Mosaic centered at  $20.0^\circ$  along the temporal horizontal meridian, in which RF centers receive signals from 6–9 cones.

tile the visual field relatively uniformly with no overlap. Figures 4B and 4C depict mosaics synthesized as  $\phi$  decreases to 0.5 and 0.0, respectively, which increasingly enforces center connections to cones of the same type. Note that this occurs at the cost of reduced spatial compactness, as is evident by the increased spatial disorder and overlap in the RF centers.

By varying  $\phi$  we can examine the effect that cone-selective pooling may have on mRGC RF spatial structure, as well as on the spatio-chromatic processing in the

369  
370  
371  
372  
373  
374  
375  
376  
377  
378  
379  
380  
381  
382  
383  
384  
385  
386  
387  
388  
389  
390  
391  
392  
393  
394  
395  
396  
397  
398  
399  
400  
401  
402  
403  
404  
405  
406  
407  
408  
409  
410  
411  
412  
413  
414

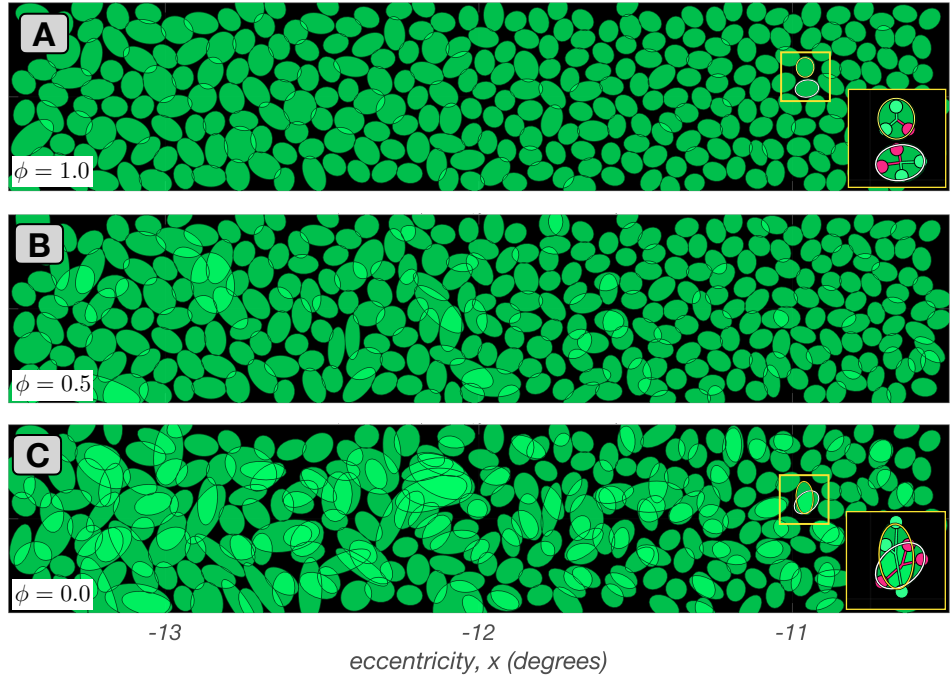
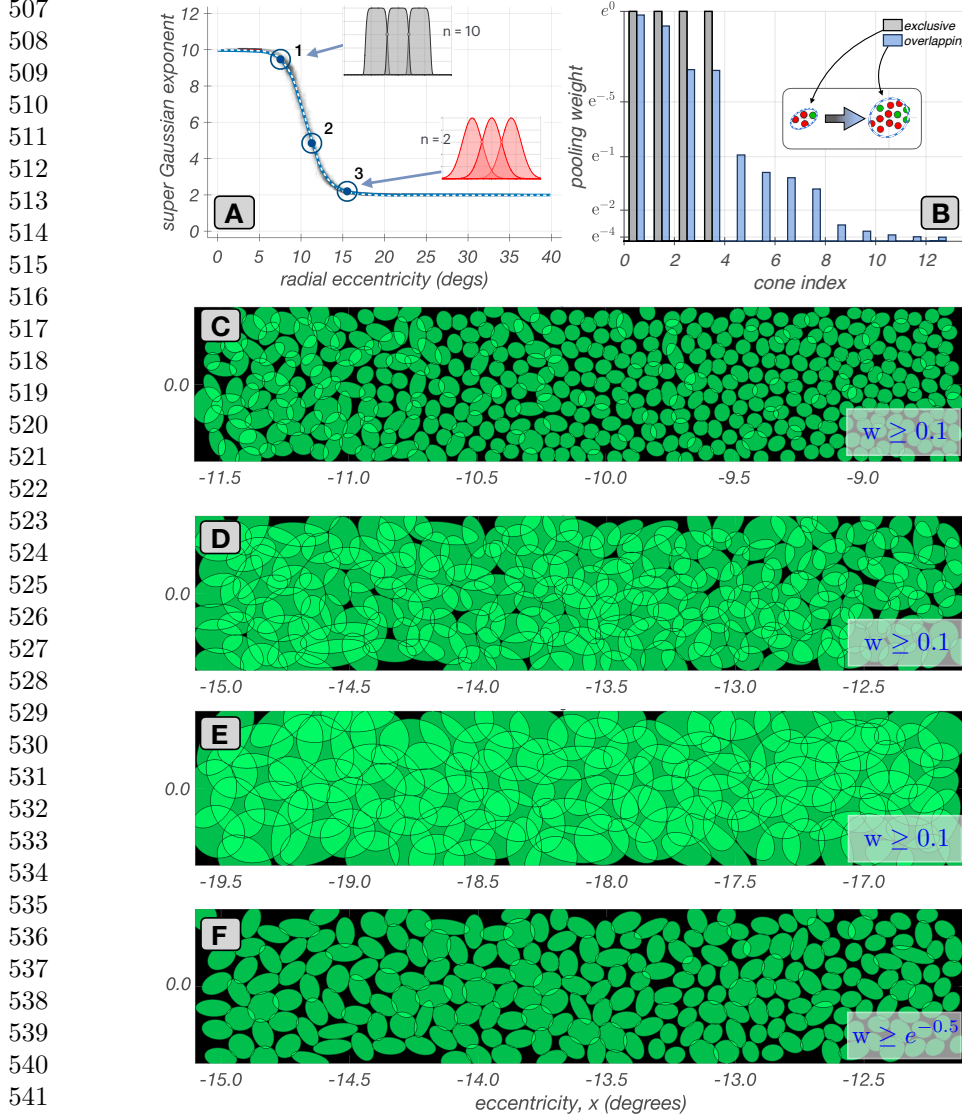


**Fig. 4 Mosaics of mRGC RF centers at the end of stage 2B.** Depicted here are  $3.0^\circ \times 0.5^\circ$  mRGC mosaics, each centered at  $12^\circ$  along the temporal horizontal meridian, but synthesized under different values of tradeoff between spatial compactness and spectral purity,  $\phi$ . **A:**  $\phi = 1.0$  (maximal spatial compactness). **B:**  $\phi = 0.5$ . **C:**  $\phi = 0$  (maximal spectral purity). Insets in A and C depict pooling of cones within the RF centers of the two mRGC RF centers contained within the yellow square. The inset in C illustrates how RF center overlap and spatial disorder is introduced as the algorithm avoids cones of different types that are close to the RF center in order to maximize the spectral purity of RF centers.

mRGC pathway. Current electrophysiological evidence favors little selective cone pooling, i.e., a  $\phi$  value of  $\approx 1$ , in RF centers of peripheral mRGCs [15, 16, 40]. However, the degree of cone type selectivity in more central locations is not known with as much certainty. For example, there is anatomical evidence that ON-center mRGCs in the fovea contact multiple ON-cone bipolars, as opposed to OFF-center mRGCs, which contact single OFF-cone bipolars [41], and also electrophysiological evidence that the RF centers of parafoveal mRGCs appear to be pooling from more than one cones [42]. In general, the question of whether foveal mRGCs that pool from more than one cone in the RF centers are doing so selectively remains unanswered. Our modeling approach allows exploration of the benefits and tradeoffs of cone-selective pooling at any retinal eccentricity, although we do not pursue such exploration in this paper.

<b>2.2.3 Mosaics with divergent cone connections (stage 2C)</b>	461
In the final substage of establishing the wiring of mRGC RF centers to the cone mosaic, the mutual exclusivity constraint is lifted and single cones are permitted to connect to multiple nearby mRGC RF centers. This divergence of cone connections is enabled by replacing the binary distribution of cone pooling weights in the mRGC RF centers with a supra Gaussian distribution, as illustrated in Fig. 5.	462
Fig. 5A depicts how a progressively increasing overlap in neighboring mRGC RF centers with eccentricity is accomplished by varying the exponent of the supra-Gaussian distribution. In central retina, the exponent is kept at 10, which results in a flat top distribution of weights with minimal overlap between neighboring RF centers (gray histograms in the inset of Fig. 5A). As eccentricity increases beyond 7°, the exponent decreases, reaching a value of 2 at around 15°, which results in Gaussian distributions of weights and a significant overlap between neighboring RF centers (red histograms in the inset of Fig. 5A).	463
To our knowledge, there is no physiological data on the variation with eccentricity of the divergence of cone connections to nearby mRGC RF centers. Therefore the varying, with eccentricity, supra-Gaussian distribution of cone weights is an arbitrary mechanism. It's intent is to capture the fact that in the fovea, input to mRGC RF centers comes exclusively or mostly [41, 42] from a single cone, whereas in the periphery, <i>in vitro</i> measurements reveal that neighboring mRGC RF centers abut at approximately one standard deviation of their Gaussian RF profile [39].	464
The transformation of cone pooling weights from binary and mutually exclusive to graduated and shared is depicted in Fig. 5B for an mRGC located at an eccentricity of 12°, with gray and blue histograms depicting the spatial distributions of cone pooling weights before and after substage 2C.	465
Figs. 5C–5E depict mosaics with divergent connections synthesized at three eccentricities. In these mosaic depictions, each green ellipse represents the spatial extent that encompasses all cones that are pooled by the RF center of a single mRGC with weights $\geq 0.1$ . For the mosaic centered at 10° (Fig. 5C), divergence of cone connections has just begun. The overlap in RF centers due to the divergence of connections increases as we move in eccentricity from 9° on the right side to 11°, on the left side. For the mosaic centered at around 13° (Fig. 5D), cone divergence and RF center overlap is higher and again increases with increasing eccentricity. For the mosaic centered at around 18° (Fig. 5E), divergence of cone connections has assymptoted, and we have a constant RF center overlap.	466
Finally, Fig. 5F provides a visualization comparable to the visualization commonly reported by <i>in vitro</i> RF mapping studies [39]. It depicts the same mosaic as Fig. 5D, but with ellipses encompassing cones that are pooled with weights $\geq e^{-1/2} \approx 0.67$ . This depiction choice makes the overlap less visually salient.	467
<b>2.3 Connecting cones to mRGC RF surrounds (Stage 3)</b>	501
<b>Overview</b>	502
In the last stage of mRGC mosaic synthesis, we derive the cone pooling weights for the mRGC RF surrounds. Since there are no clear anatomical data on surround	503
	504
	505
	506



543 **Fig. 5 Mosaics of mRGC RF centers with divergent cone connections (stage 2C).**  
 544 **A:** Variation of supra-Gaussian exponent with eccentricity. The exponent is set to 10 in the central  
 545 retina, resulting in flat top weight distributions with zero overlap (gray histograms). As eccen-  
 546 tricity is increased, the exponent is gradually decreased, achieving a value of 2.0, at around 15° (red  
 547 histograms). **B:** Transformation of cone pooling weights, from binary, in mutually exclusive con-  
 548 nections, (gray histogram) to non-binary in shared cone connections, (blue histogram) due to the  
 549 supra-Gaussian distribution for an example mRGC. Insets depict the spatial arrangement of cones  
 550 that are connected with binary and non-binary weights. **C, D & E:** Mosaics at 10°, 13°, and  
 551 18°, along the temporal horizontal meridian with divergent cone connections. The RF center ellipses  
 552 encompass the ensemble of cones with pooling weights  $\geq 0.1$ . **F:** Same mosaic as **C**, but with ellipses  
 553 showing cones with pooling weights  $\geq e^{-0.5}$ .

sizes, these weights are determined using <i>in vivo</i> characterizations of macaque mRGC visual space-referred spatial transfer functions, $vSTF(\omega)$ , i.e., the variation in response amplitude of mRGC cells as a function of spatial frequency, $\omega$ . We use the measurements of Croner & Kaplan [17], who characterized $vSTF(\omega)$ for populations of mRGCs across a wide range of eccentricities.	553
	554
	555
	556
	557
We incorporate these data into the model using numerical optimization. More specifically, we determine the cone-to-mRGC RF surround connections such that a forward simulation of the <i>in vivo</i> physiological experiments of Croner & Kaplan through the model best reproduces the experimental data. This approach allows us to use data collected through physiological optics, which blur the stimulus in an eccentricity and wavelength dependent manner, to determine the wiring of cones to mRGC RF surrounds.	558
	559
	560
	561
	562
	563
	564
Importantly, the optimization is achieved while adhering to the already established connectivity between the cone mosaic and mRGC RF centers. Simultaneously, the parametric form of the surrounds is constrained based on Packer & Dacey's characterizations of the spatial RF of macaque H1 horizontal cells [43], which are the main components of the linear spatial mRGC RF surrounds [44]. The use of optimization around forward simulation of an experiment to integrate data from multiple non-commensurate sources is an important innovation of our RGC modeling approach. Stage 3 proceeds in three sub-stages.	565
	566
	567
	568
	569
	570
	571
	572
• <b>Stage 3A:</b> We begin by computing the visual space-referred cone mosaic responses to stimuli used to measure vSTFs in macaque mRGCs. This is done by presenting achromatic gratings of different spatial frequencies which are delivered to the retina through human physiological optics [45]. We use human optics as a proxy of how macaque optics would have blurred the stimuli employed by the <i>in vivo</i> characterizations of Croner & Kaplan [17], which were collected with stimuli viewed through the animal's natural optics.	573
	574
	575
	576
	577
	578
	579
	580
• <b>Stage 3B:</b> We derive surround cone pooling functions for a subset of target synthetic mRGCs, which span the extent of the synthesized mRGC mosaic. This optimization is done so that the ensuing target cells (a) have vSTF characteristics that are well approximated by a Difference of Gaussians (DoG) model, with DoG model parameters reasonably matching the DoG model parameters reported by Croner & Kaplan at corresponding eccentricities, and (b) have surround cone pooling weights that maintain macaque H1-like spatial properties as characterized by Packer & Dacey.	581
	582
	583
	584
	585
	586
	587
	588
• <b>Stage 3C:</b> We compute surround cone pooling weights for all cells in the synthesized mRGC mosaic by evaluating the derived surround cone pooling functions at the vicinity of each mRGC's input cone mosaic and finally interpolating the computed weights. A small amount of jitter in the ratio of the surround to center weights is added to simulate the variance in integrated surround to center ratio at each eccentricity seen in the macaque data.	589
	590
	591
	592
	593
	594
	595
	596
	597
	598

599 **2.3.1 Computation of visual space-referred cone mosaic responses**  
600       **to stimuli used to measure vSTFs in macaque mRGCs**  
601       **(Stage 3A)**

602 We employ the ISETBio machinery to compute the excitation of the input cone mosaic  
603 to achromatic gratings of different spatial frequencies delivered to the retina via phys-  
604 iological optics. This process captures several crucial spatio-chromatic effects in the  
605 transformation of scene radiance into cone responses: spatial and chromatic filtering  
606 by physiological optics, spectral filtering by the eye's inert pigments, and sampling by  
607 the interdigitated trichromatic cone mosaic. To mimic the phototransduction process,  
608 cone excitation responses are converted to cone modulation responses.

610 In these computations, we employ human physiological optics matched to the  
611 eccentricity of each synthesized mRGC, but we adjust the defocus term of the mod-  
612 eled optics so as to maximize the Strehl ratio. The Strehl ratio is defined as the ratio  
613 of peak sensitivity of the point spread function (PSF) at the wavelength of focus, here  
614 550 nm, to the peak sensitivity of a diffraction-limited PSF. This is done as a proxy to  
615 the experimental paradigm of Croner & Kaplan, in which corrective lenses were used  
616 to maximize cell responses at high spatial frequencies (personal communication with  
617 the late Ehud Kaplan).

618 **619 2.3.2 Deriving surround cone pooling functions for a subset of**  
620       **target synthetic mRGCs (Stage 3B)**

621 Croner & Kaplan reported summaries of spatial RF characteristics across populations  
622 of mRGCs at different eccentricities which were derived by fitting a DoG model to the  
623 measured vSTF. The DoG model defined in spatial frequency,  $\omega$ , domain is given by:

625 
$$\text{DoG}(\omega) = K_c \cdot R_c^2 \cdot \exp[-\pi \cdot R_c \cdot \omega]^2 - K_s \cdot R_s^2 \cdot \exp[-\pi \cdot R_s \cdot \omega]^2 \quad (1)$$

627 where  $K_c$  and  $K_s$  are the peak sensitivities of the RF center and RF surround mecha-  
628 nisms, and  $R_c$  and  $R_s$  are the corresponding characteristic radii. The vSTF of a typical  
629 macaque mRGC is depicted in Fig. 6A with cyan disks. The solid heavy line depicts  
630 the fitted DoG model, with the center and surround components depicted by the thin  
631 solid and dashed lines, respectively.

632 The shape of the vSTF is determined by two key measures, the ratio of surround  
633 to center characteristic radii,  $R_s/R_c$ , and the ratio of surround to center integrated  
634 sensitivities,  $K_s/K_c \times (R_s/R_c)^2$ . The distributions of these two ratios as a function of  
635 eccentricity in the population of mRGCs recorded by Croner & Kaplan are depicted  
636 by the gray squares in Figs 6B1 & 6B2. The mean variation in these two ratios, shown  
637 as dashed lines, are the target values used to derive the surround cone pooling weights  
638 in the synthetic mRGCs.

639 The optimization process is illustrated schematically in Fig. 6C. The vSTF of  
640 the target synthetic mRGC is computed by forward simulation of the experiment of  
641 Croner & Kaplan. The time course of responses of L- and M-cones in the input cone  
642 mosaic to a drifting grating stimulus of spatial frequency  $\omega$ ,  $R_{\text{cones}}(\omega, t)$ , (computed  
643 in Stage 3A) are depicted by the red and green traces in the rectangular panel of

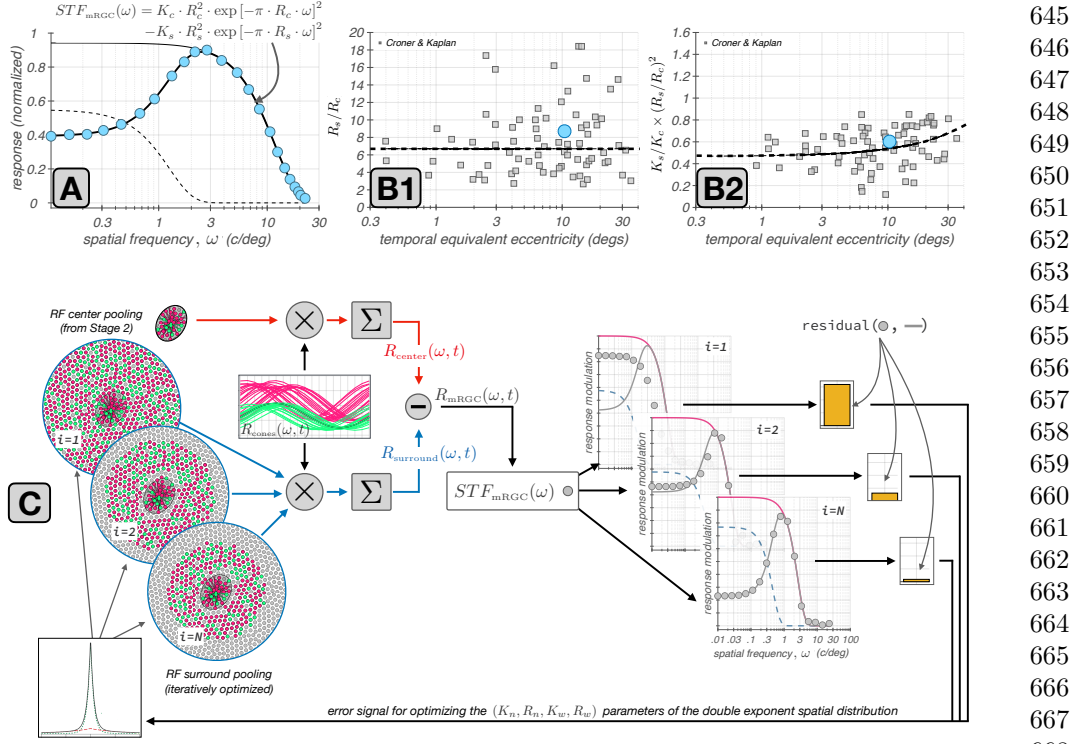


**Fig. 6 Derivation of cone weights to mRGC surrounds.** **A:** Typical macaque mRGC vSTF (cyan disks) fitted with a Difference of Gaussians model (thick black line), whose center and surround components are depicted by the thin black and the dashed line, respectively. **B1 & B2:** Ratios of surround to center characteristic radii,  $R_s/R_c$ , and ratios of surround to center integrated sensitivities,  $K_s/K_c \times R_s^2/R_c^2$  as a function of eccentricity in the population of mRGCs recorded by Croner & Kaplan [17]. The dashed lines represent the trends in these two ratios as a function of eccentricity. The cyan disks depict the ratios for the example vSTF depicted in A. **C:** Depiction of the iterative estimation of surround cone pooling weights by forward simulation of the Croner & Kaplan vSTF measurements. See description in text for more details.

Fig. 6C. A spatially weighted sum of these cone responses using the RF center cone pooling weights (computed in Stage 2), is used to compute the response of the RF center,  $R_{\text{center}}(\omega, t)$ . This operation, which is depicted by the red computation arm in Fig. 6C, is fixed throughout the optimization of the surround.

In the computation of the spatial distribution of surround cone pooling weights, we impose a parametric form that is described by the sum of a narrow and a wide exponential spatial component, based on characterizations of the spatial RF properties of H1 horizontal cells by Packer & Dacey [43]. Specifically,

$$W_s(r) = K_{\text{wide}} \times \exp[-r/R_{\text{wide}}] + K_{\text{narrow}} \times \exp[-r/R_{\text{narrow}}] \quad (2)$$

where  $r$  is the radial distance from the RF center,  $K_{\text{wide}}$  and  $K_{\text{narrow}}$  are the peak sensitivities of the wide and the narrow components, respectively, and  $R_{\text{wide}}$  and  $R_{\text{narrow}}$  are the corresponding characteristic radii.

691 Beginning with a random initial value for the parameters of the double exponential  
692 distribution, we compute an initial estimate of the surround cone weights by evalu-  
693 ating  $W_s(r)$  at the vicinity of the input cone mosaic that surrounds the RF center.  
694 These weights are depicted in the top-left circular panel of Fig. 6C (labeled as  $i = 1$ ,  
695 with  $i$  denoting iteration). Using these initial weights we compute a weighted sum of  
696 the surround cone responses to derive the initial estimate of the surround response,  
697  $R_{\text{surround}}(\omega, t)$ . This operation is depicted by the blue computation arm in Fig. 6C.

698 The composite response of the synthesized mRGC is obtained by instantaneously  
699 subtracting the surround response from the center response, as follows:

700

$$R_{\text{mRGC}}(\omega, t) = R_{\text{center}}(\omega, t) - R_{\text{surround}}(\omega, t) \quad (3)$$

702

703 The amplitude modulation of  $R_{\text{mRGC}}(\omega, t)$  is taken as the value of the cell's  
704 vSTF<sub>mRGC</sub>( $\omega$ ). Repeating over a range of spatial frequencies, we obtain the initial  
705 estimate of the full vSTF<sub>mRGC</sub>, which is depicted by the gray disks in the top-right  
706 rectangular panel of Fig. 6C, labeled as  $i = 1$ .

707 Following the experimental procedure of Croner & Kaplan, we fit the computed  
708 vSTF<sub>mRGC</sub>( $\omega$ ) with a DoG model. This fit is depicted by the solid gray line in the top-  
709 right rectangular panel of Fig. 6C. Note that in this procedure we constrain the DoG  
710 model fit so that its shape parameters,  $R_s/R_c$ , and  $K_s/K_c \times R_s^2/R_c^2$ , both lie within  
711 a narrow range of the mean values of  $R_s/R_c$ , and  $K_s/K_c \times R_s^2/R_c^2$  ratios reported  
712 for macaque mRGCs at corresponding eccentricities [17]. Due to this constrain, in the  
713 first iteration the residual between the computed vSTF and the DoG model fit to it,  
714 is large.

715 This residual  $\|v\text{STF}_{\text{mRGC}} - \text{DoG}\|$ , depicted by the yellow bar in the right-most  
716 panel of Fig. 6C, serves as an error signal. The optimization algorithm minimizes  
717 this error signal by adjusting the parameters of  $W_s(r)$ , which controls the surround  
718 weights. This adjustment is also constrained, so that the parameters of  $W_s(r)$  remain  
719 within a range of the values reported in macaque H1 horizontal cells [43].

720 When the  $\|v\text{STF}_{\text{mRGC}} - \text{DoG}\|$  reaches a minimum value, labeled as  $i = N$ ,  
721 in Fig. 6C, we obtain the optimized surround cone pooling function for the target  
722 synthetic mRGC. Additional details about this surround optimization method are  
723 provided in Supplemental Section B.1.

724

## 725 2.4 Deriving surround cone pooling weights for each cell in 726 the mosaic(stage 3C)

727

728 The optimization of the surround cone pooling functions is a computationally expensive  
729 process. It is therefore conducted on a sparse spatial grid (with  $N_{xy}$  nodes), which  
730 encompasses the spatial extent of the synthesized mRGC mosaic. At each node of the  
731 spatial grid, we determine the range of cone numerosities in the RF centers of nearby  
732 synthetic mRGCs, and we derive optimized surround cone pooling functions for each  
733 of the encountered RF center cone numerosities ( $N_c$ ), and we do this twice, once for  
734 L-cone dominated RF centers, and once for M-cone dominated RF centers.

735 Once these  $N_{xy} \times N_c \times 2$  surround cone pooling functions are derived, we compute  
736 surround cone pooling weights for all synthetic mRGCs. For each target mRGC we

determine the 3 nearest spatial grid nodes, and extract the optimized surround cone	737
functions that were derived at this node for the cone numerosity that matches that	738
of the target mRGC, for both L- and M-center cone dominance variants. Then we	739
evaluate the six optimized surround pooling functions at the input cone mosaic in the	740
vicinity of the target mRGC, deriving six sets of surround cone pooling weights. The	741
target cell's surround cone pooling weights are determined by interpolating the 6 sets	742
of weights spatially, weighted inversely proportionally by the distance between the	743
location of the target mRGC and the location of the optimized model, and spectrally,	744
weighted based on the relative L-/M- cone weight ratio in the RF center of the target	745
mRGC.	746
	747
<b>2.4.1 Adjusting the surround pooling variance</b>	748
The final step in the generation of the mRGC RF surrounds is to apply a noisy scalar	749
multiplier to all surround pooling weights of individual mRGCS. The value of this	750
scalar is chosen so that the variance in the ratio of surround to center integrated sensi-	751
tivities, $K_s/K_c \times (R_s/R_c)^2$ , of the synthetic mRGCS matches the variance observed in	752
the population of macaque mRGCS recorded by Croner & Kaplan. The manipulation	753
in $K_s/K_c \times (R_s/R_c)^2$ variance does not require re-computing the surround pooling	754
functions. This is unlike manipulating the variance in the $R_s/R_c$ ratio, which requires	755
re-computing the surround pooling functions.	756
	757
	758
<b>2.5 Computing mRGC responses from cone mosaic responses</b>	759
A fully synthesized mRGC mosaic consists of two connectivity matrices: $P_{center}(i, k)$ ,	760
determined in synthesis stage 2, and $P_{surround}(i, k)$ , determined in synthesis stage	761
3, which capture the weights by which the RF center and surround mechanisms,	762
respectively, of the $k^{th}$ - cell in the mRGC mosaic pools signals from the $i^{th}$ cone in	763
the input cone mosaic.	764
Since the current version of the mRGC model does not contain a temporal compo-	765
nent, the response of the $k^{th}$ mRGC to some stimulus at time instant, $t$ , $R_{stim}(k, t)$ ,	766
is computed instantaneously from the response of the input cones to that stimulus at	767
time $t$ , $C_{stim}(i, t)$ , as follows:	768
	769
$R_{stim}(k, t) = \frac{1}{\sum_{i=1}^n P_{center}(i, k)} \times \dots$	770
$\left( \sum_{i=1}^n P_{center}(i, k) \cdot C_{stim}(i, t) - \sum_{j=1}^m P_{surround}(j, k) \cdot C_{stim}(j, t) \right)$	771
	772
	773
	774
	775
	776
	777
To mimic adaptation to the background stimulus, the mRGC mosaic typically oper-	778
ates on cone contrast responses, instead of cone excitation responses, so the $C_{stim}(i, t)$	779
	780
	781
	782

783 term in the above equation is computed as follows:

784

785 
$$C_{\text{stim}}(i, t) = \frac{E_{\text{stim}}(i, t) - E_{\text{bkgnd}}(i)}{E_{\text{bkgnd}}(i)}$$
 (5)

786

787 where  $E_{\text{stim}}(i, t)$  is the excitation response of the  $i^{\text{th}}$  cone to the examined stimulus at  
788 time  $t$ , and  $E_{\text{bkgnd}}(i)$  is that cone's excitation response to a uniform field, zero con-  
789 trast stimulus, whose mean chromaticity and luminance match those of the examined  
790 stimulus.

791

### 792 3 Results

793

794 A key feature of our model is its dual representation of mRGC receptive field (RF)  
795 properties, which separates neural circuitry from optical effects. The first representa-  
796 tion, in *retinal space*, models the direct pooling of cone signals by the RF center and  
797 surround. This describes the cell's intrinsic spatio-chromatic filtering and is directly  
798 comparable to anatomical data and physiological measurements that bypass the eye's  
799 optics (e.g., *in vitro* or adaptive optics experiments [10, 46]). In contrast, the second  
800 representation, in *visual space*, models the end-to-end processing of a stimulus as it  
801 passes through the eye's optics to the mRGC mosaic. This representation is applicable  
802 to conventional *in vivo* physiology and psychophysical assessments of visual function.

803 The ability to go back and forth between cone and visual space is critical to under-  
804 standing how retinal cone pooling interacts with physiological optics to generate the  
805 processing characteristics of cells in visual space, which is what ultimately determines  
806 natural visual performance. This ability is also critical in interpreting results from *in*  
807 *vivo* physiology in terms of the underlying retinal wiring [31], as well as to relating  
808 results obtained under adaptive optics viewing conditions to results obtained under  
809 natural viewing conditions [10].

810 In this section we illustrate and contrast spatial RF characteristics of synthetic  
811 mRGCs in the two representations and validate the properties of synthetic mRGCs  
812 against those of macaque mRGCs as characterized by *in vivo* and *in vitro* physiological  
813 studies.

814

#### 815 3.1 Spatial characteristics of synthesized mRGC receptive 816 fields

817

818 Spatial characteristics of cells in an mRGC mosaic synthesized at  $4.5^{\circ}$  along the tem-  
819 poral horizontal meridian are depicted in Fig. 7. The employed mosaic is depicted in  
820 Fig. 7A. The numbered positions in Fig. 7A identify the locations of three selected  
821 cells whose spatial RF characteristics are explored in detail next.

822 The cone pooling maps of these exemplar mRGCs are depicted in Figs 7B1–B3.  
823 Here, pink and cyan disks depict L- and M-cones, respectively, that are pooled by  
824 the RF center with a weight  $\geq 0.1$ , or by the RF surround with a pooling weight  $\geq$   
825 0.005, and gray disks depict cones that are either not pooled at all or pooled with  
826 a weight less than the threshold for labeling. The solid and dashed lines depict the  
827 spatial pooling extents of the RF center and surround mechanisms, respectively.

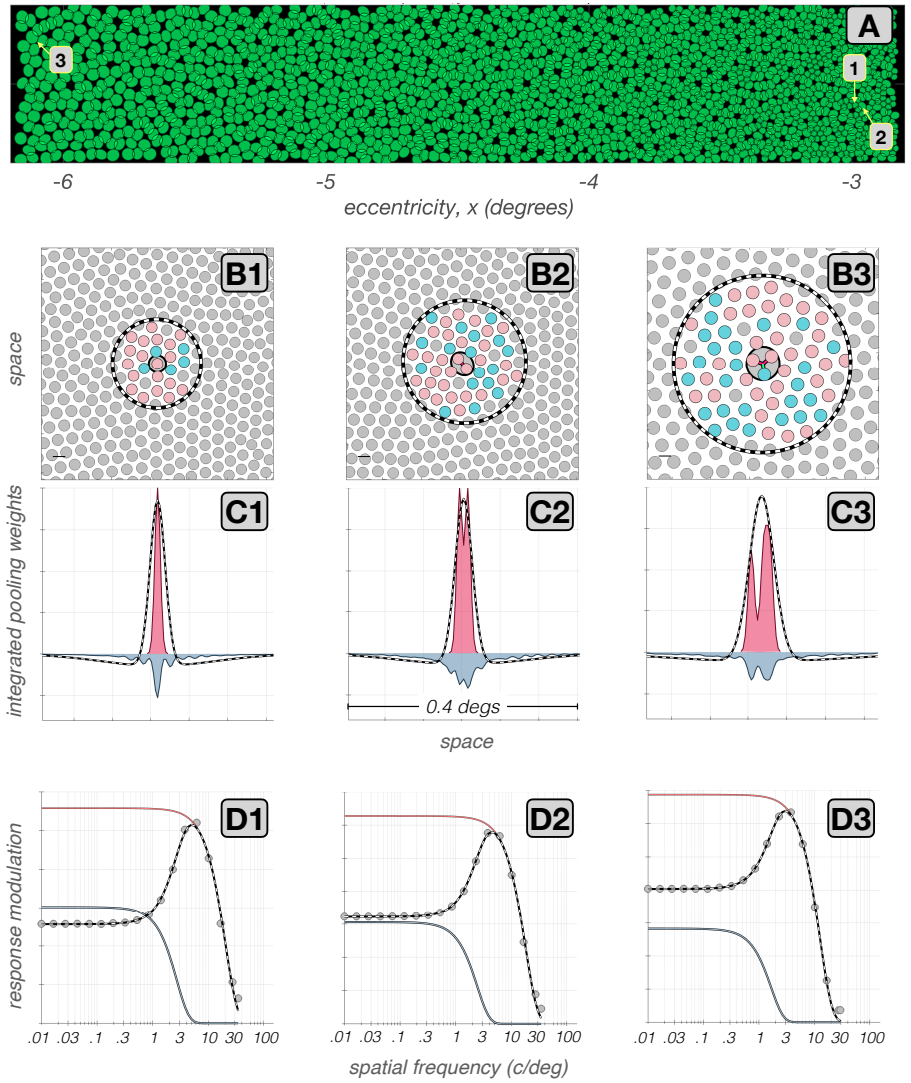


**Fig. 7 Spatial RF characteristics of synthetic mRGCs** **A:** Mosaic of RF centers of an mRGC mosaic synthesized at  $4.5^\circ$  along the temporal horizontal meridian. **B1–B3:** Cone pooling maps for 3 exemplar cells whose positions within the mRGC mosaic are labeled in A. Pink and cyan disks depict L- and M-cones, respectively, with RF center pooling weights  $\geq 0.1$ , or with RF surround weights  $\geq 0.005$ . Gray disks represent either S-cones, which are not pooled in our model, or L-/M-cones with pooling weights lower than the labeling thresholds. The solid and dashed black lines depict the extents of the RF center and surround pooling regions. **C1–C3:** Y-axis integrated cone pooling weight profiles within the RF center (maroon) and surround (slate). The dashed lines depict the visual space-referred line weighting functions as derived by fitting Difference of Gaussians (DoG) models to each cell's vSTF. **D1–D3:** The vSTFs of the exemplar mRGCs, computed under physiological optics, are depicted by the gray disks. The gray lines depict the DoG model fits to these vSTFs, and the maroon and slate lines depict the models' center and surround components, respectively.

875 The cell depicted in Fig. 7B1 is located at an eccentricity of  $3^\circ$ . Its RF center  
876 pools from a single L-cone and its RF surround pools from a total of 16 L- and M-  
877 cones. The cell depicted in Fig. 7B2, also located at  $3^\circ$ , pools from two L-cones in its  
878 RF center, and its RF surround is larger, pooling from 44 L- and M-cones. The cell  
879 depicted in Fig. 7B3 is located at  $6^\circ$ . Its RF center, which pools from 2 L-cones and  
880 1 M-cone, and its surround are both larger than those of the first 2 cells. The cone  
881 pooling maps depicted in Figs 7B1–B3 illustrate the spatial connectivity between the  
882 input cone mosaic and the center and surround subregions of mRGC RFs, but do not  
883 depict the strength of these connections. In this sense, these maps depict the type of  
884 information that is available from detailed anatomical studies.

885 Figs 7C1–C3 add to this view by providing information about the strength of the  
886 cone inputs for the three exemplar cells. Here, the maroon and slate histograms depict  
887 the cells' spatially integrated (along the y-axis) cone pooling weights for the RF center  
888 and the surround mechanisms, respectively. Note that in the cell depicted in Fig. 7C1,  
889 the double exponential spatial profile of the surround cone pooling mechanism, with  
890 a sharp peak around the RF center and more shallow weights in peripheral regions, is  
891 prominent. In the two other cells shown, this feature is less prominent.

892 This observation, where cells with larger RF centers have less peaked surround  
893 weights than cells with smaller RF centers is seen commonly in our synthetic mRGCs.  
894 The variation in surround pooling characteristics with RF center size results from  
895 constraints in the model, which maintain vSTF shape parameters that are consistent *in*  
896 *vivo* measurements [17] while at the same time remaining consistent with the surround  
897 parametric form indicated by measurements of H1 receptive fields [43].

898 Visual space-referred spatial transfer functions are commonly measured in *in vivo*  
899 physiological assessments to estimate spatial RF properties of mRGCs [17, 18]. The  
900 vSTFs of the three examined synthetic mRGCs are depicted by the gray disks in  
901 Figs 7D1–7D3. The corresponding DoG model fits are depicted by the solid gray lines,  
902 and the spatial RF profiles corresponding to these DoG model fits are depicted by the  
903 dashed lines in Figs 7C1–C3. Contrasting these inferred spatial RF profiles with the  
904 actual cone pooling profiles, it becomes evident that one cannot use characterizations  
905 obtained under physiological optics viewing to directly infer the characteristics of  
906 spatial pooling of cone signals in the retina. We discuss this issue further in later  
907 sections.

908

### 909 3.2 Validation against *in vivo* physiology across the visual field

910

911 To validate our model, we synthesized mRGC mosaics across a wide region of the  
912 retina, and computed vSTFs of individual mRGCs by probing them with drifting  
913 achromatic gratings of different spatial frequencies delivered to the retina under phys-  
914 iological optics appropriate for the eccentricity of the examined cells, simulating the  
915 experimental paradigm of Croner & Kaplan [17].

916

917 To compare synthetic and macaque mRGCs we fitted the synthetic cell vSTFs  
918 with the DoG model employed by Croner & Kaplan and compared the ratios of sur-  
919 round to center characteristic radii,  $R_s/R_c$ , and ratios of surround to center integrated  
920 sensitivities,  $K_s/K_c \times R_s^2/R_c^2$ , to those reported by Croner & Kaplan.

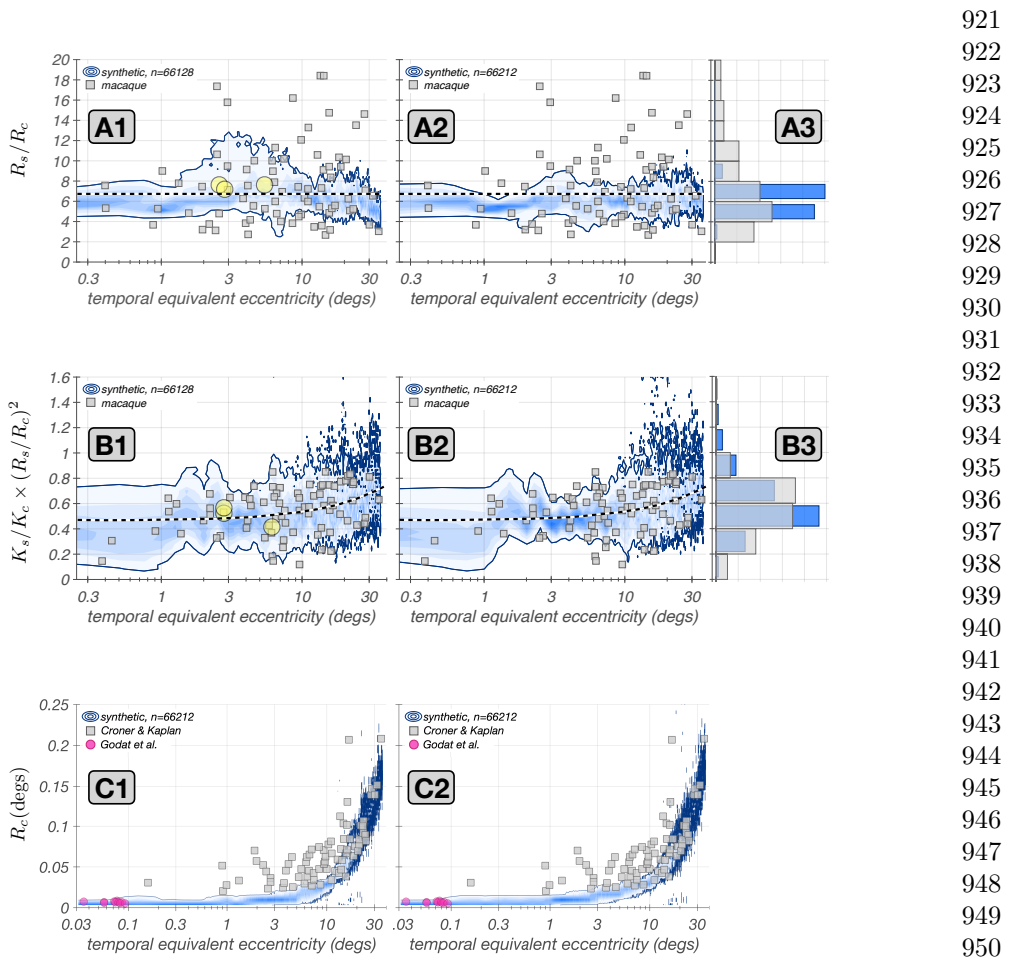


**Fig. 8 Validation against *in vivo* measurements.** In all panels, gray squares depict data from the population of macaque mRGCs recorded by Croner & Kaplan [17]. Blue contours depict the probability density function of the examined parameter in a population of 66,128 synthetic mRGCs with color saturation encoding probability level. Solid blue lines represent the 5% – 95% percentile range of examined parameter. Left and right panels are for mosaics synthesized under physiological optics of two different human subjects. **A1–A2:** Correspondence in ratio of surround-to-center characteristic radii,  $R_s/R_c$ , across eccentricity. The dashed line represents the target value that is in effect during the optimization of the synthetic mRGC surrounds, which is the mean value of  $R_s/R_c$  across the population of all mRGCs recorded by Croner & Kaplan. **A3:** Marginal histograms of  $R_s/R_c$  for macaque (gray) and synthetic mRGCs (blue). **B1–B2:** Correspondence in ratio of surround-to-center integrated sensitivities,  $K_s/K_c \times (R_s/R_c)^2$ , across eccentricity. The dashed line represents the target values in effect during the optimization of the synthetic mRGC surrounds, which is the trend observed with eccentricity in the population of the macaque mRGCs recorded by Croner & Kaplan. **B3:** Marginal histograms of  $K_s/K_c \times (R_s/R_c)^2$  for macaque (gray) and synthetic mRGCs (blue). **C1–C2:** Correspondence in RF center characteristic radius,  $R_c$ , across eccentricity. The fuschia disks represent the  $R_c$  of foveolar mRGCs recorded by Godat *et al.* [10], back-projected in visual space using the monkey's own physiological optics.

921  
922  
923  
924  
925  
926  
927  
928  
929  
930  
931  
932  
933  
934  
935  
936  
937  
938  
939  
940  
941  
942  
943  
944  
945  
946  
947  
948  
949  
950  
951  
952  
953  
954  
955  
956  
957  
958  
959  
960  
961  
962  
963  
964  
965  
966

967 The results of this analysis are depicted in Fig. 8, in which the left and right  
968 panels depict data from mRGC mosaics synthesized under the physiological optics  
969 of two different human observers. Figs. 8A1 and 8A2 compare the distribution of  
970  $R_s/R_c$  ratios. Gray squares depict the macaque mRGC data and the blue density plots  
971 depict the 5%–95% percentile range of the  $R_s/R_c$  ratios in a population of 66,128  
972 synthetic mRGCs. The three yellow disks in Fig. 8A1 correspond to the three exemplar  
973 cells illustrated in Fig. 7. Note that the  $R_s/R_c$  ratios in synthetic mRGCs follow the  
974 macaque data across eccentricity for both human subjects. The synthetic data do  
975 not, however, capture the full variance seen in the macaque data, as is evident by  
976 the marginal histograms (Fig. 8A3). To capture the full variance seen in the macaque  
977 data, we could consider synthesizing multiple surround pooling functions, each with  
978 different target values of  $R_s/R_c$ , and then randomly selecting for each synthesized  
979 mRGC from the multiple sets.

980 On the other hand, the integrated sensitivity ratios,  $K_s/K_c \times R_s^2/R_c^2$ , of the  
981 synthetic mRGC population, depicted in Figs 8B1–B3, capture both the trend with  
982 eccentricity and the variance of the macaque data. The variance match was achieved  
983 by enforcing a target variance in the  $K_s/K_c \times R_s^2/R_c^2$  ratio of the synthetic cells as  
984 described earlier.

985 Note that, although we did use the mean variation with eccentricity of macaque  
986  $R_s/R_c$  and  $K_s/K_c \times R_s^2/R_c^2$  ratios during construction of the model, the model was  
987 derived using additional constraints: those imposed by the densities of cones and  
988 mRGC RFs, by the spatial characteristics of H1 horizontal cells, and by the influence  
989 of human optics. These validations, therefore, check both that we have not over con-  
990 strained our model in a manner that makes it inconsistent with the macaque data,  
991 and that our method of interpolating surround pooling weights from models derived  
992 at a set of discrete retinal locations works well.

993 We next examined the correspondence between synthetic and macaque mRGCs in  
994 terms of their visual space-referred RF center sizes,  $R_c$ . Recall that in synthesizing  
995 mRGC mosaics, the RF centers are constructed independently of the Croner & Kaplan  
996 physiological data, using only anatomical data and estimates of RF center overlap  
997 obtained from *in vitro* physiology in the periphery [39]. Figs. 8C1–C2 compare the  
998 distributions of  $R_c$  between the macaque and synthetic mRGCs. Note that  $R_c$  in the  
999 synthetic mRGCs follows the trend seen in macaque mRGCs with eccentricity, with  
1000 good agreement at eccentricities above 10° for both subjects. In more central locations,  
1001 however, the synthetic mRGC RF center sizes are 2–3 times smaller than those in the  
1002 macaque. We believe that the discrepancy at central locations is not a deficiency of  
1003 our model, but rather results from several factors.

1004 First, the cone mosaic in our model has a peak density of 288,000 cones/mm<sup>2</sup>  
1005 which is near the high end of densities reported in humans [36], whereas the average  
1006 macaque peak cone density is around 200,000 cones/mm<sup>2</sup> [47, 48]. The higher cone  
1007 mosaic density in humans implies smaller cone apertures, which in turn would bias  
1008 our synthetic mRGCs towards somewhat smaller RF centers.

1009 Second, in acute macaque experiments, optical refraction is not necessarily perfect,  
1010 so there could be residual blur due to errors in refraction, as well as due to corneal  
1011 edema from the contact lens used in typical multi-day acute experiments. This would  
1012

increase the size of the RF centers in the physiological data relative to those in our model in central retina. Moreover, residual eye movements can occur in acute experiments, despite the ocular muscle paralysis (personal observations by N.P. Cottaris). Such residual movements would artificially enlarge estimates of RF center size for central retina mRGCs.

Finally, in the macaque mRGC vSTF characterizations of Croner & Kaplan, stimulus orientation was not optimized to match any orientation bias in the RF of macaque mRGCs (Lisa Croner, personal communication), whereas in the simulated experiments, stimulus orientation was matched to the cell's visual-space referred orientation bias, which results in the smallest possible estimate of RF center size. Indeed, in additional analyses (not shown) in which we computed vSTFs under random grating orientations as well as a fixed orientation (as was done by Croner & Kaplan), we found enlarged estimates of  $R_c$ . However, these enlarged estimates still fall short of those reported by Croner & Kaplan, so the first two factors that we mentioned above must also be at play.

Support for our assertion is provided by *in vivo* data from foveal macaque mRGC vSTFs obtained under adaptive optics viewing conditions [10]. The center sizes of these cells, blurred by the optics measured for the monkey subjects studied, are depicted by the purple disks in Figs. 8C1 & 8C2. Note that these align well with the  $R_c$  values of our synthetic mRGCs.

### 3.3 Validation against *in vitro* physiology in the periphery

We also compared spatial RF properties of synthetic mRGCs against macaque data from *in vitro* mRGC recordings. Since the *in vitro* data are not subject to optical blur, they may be compared directly to the retinal-space characteristics of our model. Data of this sort are currently only available in the peripheral retina.

The first study considered is that of Gogliettino *et al.* [49], in which the spatial RFs of mosaics of macaque mRGCs were mapped using white noise stimulation. To simulate their experiments, we probed synthetic mRGCs with white noise modulated achromatic checkerboard stimuli delivered to the retina under diffraction limited optics. To compute the spatial RFs of synthetic mRGCs, we cross-correlated the synthetic mRGC responses with the white noise stimulus sequence. Results of this analysis are depicted in Fig. 9.

The spatial RFs of cells in synthetic mRGC mosaics at three eccentricities, 3.5 mm, 6.75 mm and 8.5 mm, are illustrated by the black ellipses in the three top panels of Fig. 9A. The superimposed green filled ellipses depict spatial RFs from macaque mRGC mosaics located at 3.5 mm and 8.5 mm. Note that at both eccentricities, there is good correspondence in RF center size and coverage between the synthetic and the macaque mRGC mosaics.

To quantify the retinal space-referred RF center sizes in synthetic mRGCs, we computed the diameter of their RF centers as  $2 \times \sqrt{\sigma_{\text{minor}} \times \sigma_{\text{major}}}$ , where  $\sigma_{\text{minor}}$  and  $\sigma_{\text{major}}$  are the standard deviations of the fitted Gaussian ellipsoid along its minor and major axes. The results of this analysis across eccentricity are depicted by the black dots in Fig. 9C, along with the RF center sizes of mosaics of macaque mRGCs located at 3.5 mm and 8.5 mm, which are depicted by the green squares.

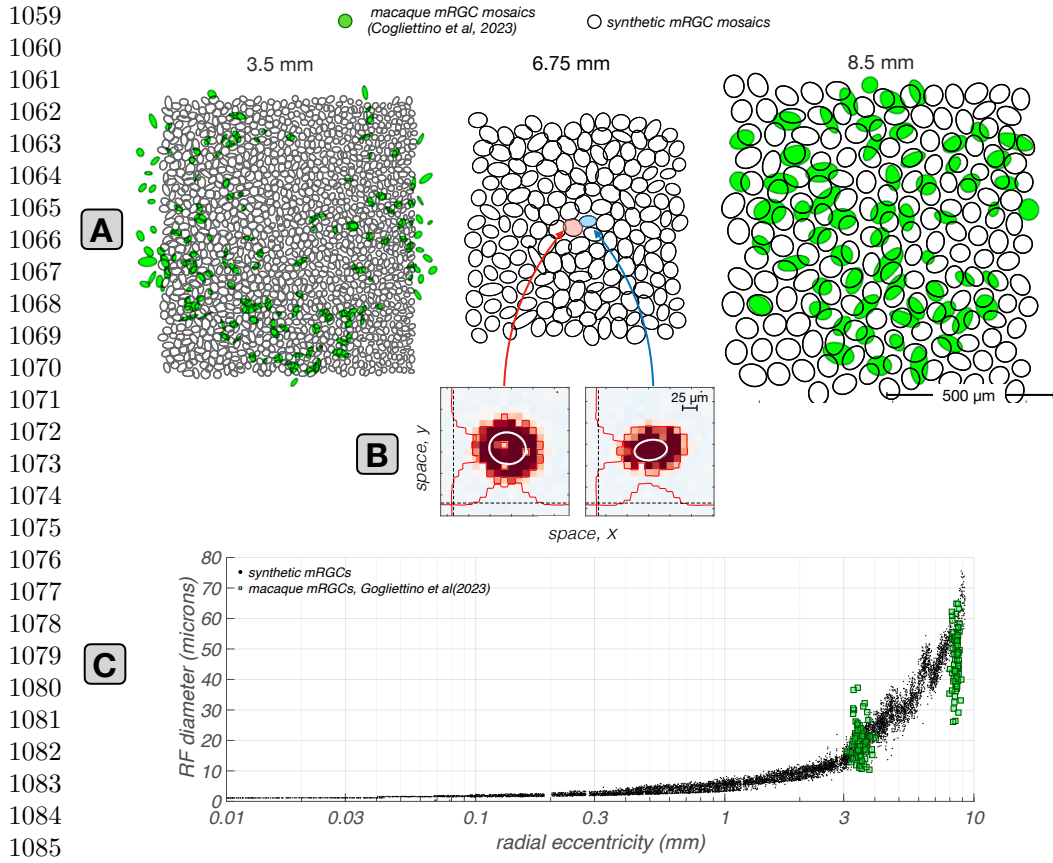


**Fig. 9 Retinal space-referred RF center sizes: synthetic vs. macaque mRGCs recorded *in vitro*.** **A:** Mosaics of synthetic mRGCs synthesized at three eccentricities, 3.5, 6.75, and 8.5 mm along the temporal meridian. The black contours depict Gaussian ellipsoid fits to the increment-excitatory regions of the computed RF maps, drawn at the  $e^{-1}$  normalized sensitivity level. Only the increment-excitatory region of the RF map is fitted. Green contours depict RF maps from two macaque mRGCs mosaics from the *in vitro* recordings of Gogliettino et al. [49]. **B:** Example spatial RF maps of two synthetic mRGCs located at 6.75 mm, computed via white noise stimulation delivered to the retina under diffraction limited optics. Regions excitatory to light increments, i.e. the RF centers, and to light decrements, i.e., the RF surrounds, are indicated by red and blue colors, respectively. The scattered zero excitation spots within the light-increment RF centers correspond to the location of S-cones. White lines depict iso-contour plots of Gaussian ellipsoids fitted to the light increment-excitatory RF center region, drawn at the  $e^{-1}$  normalized sensitivity level. **C:** Comparison of synthetic against macaque mRGC RF center sizes across eccentricity. Black dots depict the RF diameters of synthetic mRGCs, computed from the Gaussian ellipsoid fits as  $2 \times \sqrt{\sigma_{\text{minor}} \times \sigma_{\text{major}}}$ , and green squares depict the RF diameters of macaque mRGCs at the two eccentricities where the *in vitro* measurements are available.

Note that the correspondence between synthetic and macaque data is excellent at 3.5 mm, whereas at 8.5mm, the RF diameters of the synthetic mRGCs are, on average, 30–40% larger than the RF diameters of macaque mRGCs. The deviation in RF size at the far periphery may occur because human and macaque retinas differ somewhat

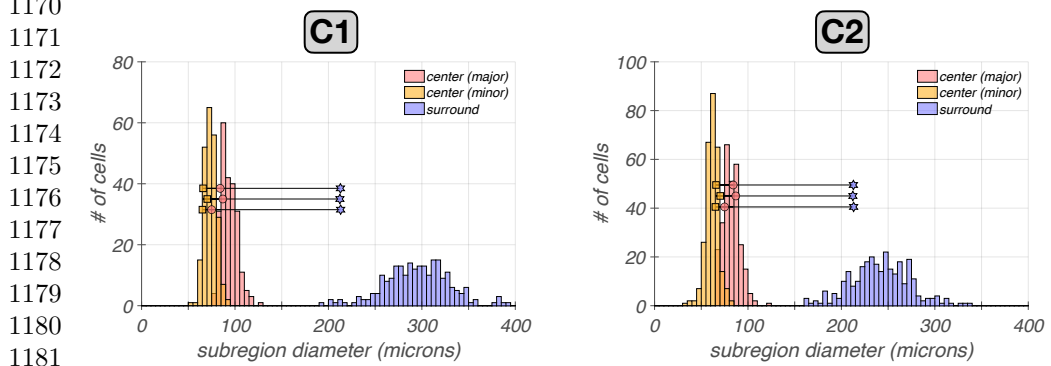
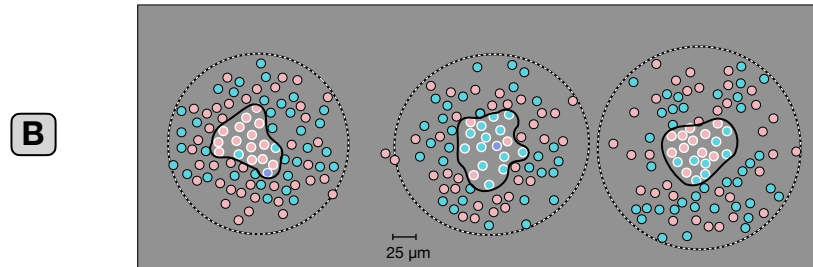
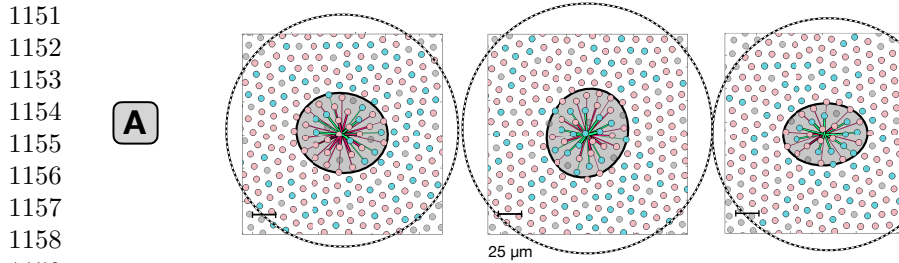
in the periphery. For example, in the human retina, cone density does not change much for eccentricities > 5mm, whereas in the macaque retina it continues to drop as eccentricity increases [50]. The RF size deviation we observe could be the result of a higher mRGC density in the peripheral macaque retina, relative to the human retina. 1105  
1106  
1107  
1108  
1109  
1110  
1111  
1112  
1113  
1114  
1115  
1116  
1117  
1118  
1119  
1120  
1121  
1122  
1123  
1124  
1125  
1126  
1127  
1128  
1129  
1130  
1131  
1132  
1133  
1134  
1135  
1136  
1137  
1138  
1139  
1140  
1141  
1142  
1143  
1144  
1145  
1146  
1147  
1148  
1149  
1150

The second *in vitro* study we validated our synthetic mRGCs against, is that of Field *et al.* [15], which examined the spatial layout of single cone inputs to the RF centers and surrounds in peripheral macaque mRGCs. Results of this comparison are depicted in Fig. 10. The cone pooling maps of three synthetic mRGCs at a temporal eccentricity of 6.75 mm are depicted in Fig. 10A. The spatial distribution of cone pooling weights in three macaque mRGCs at the same eccentricity from the study of Field *et al.* [15], adapted from their Fig. 4, are shown in Fig. 10B. For both synthetic and macaque mRGCs, the visualized surround cones have pooling weights > 0.005 × the peak center cone weight (Greg Field, personal communication).

Note the general agreement between synthetic and macaque mRGCs in the extent of both their RF centers and surrounds, although again, synthetic mRGCs appear to have slightly larger RFs than their macaque counterparts. Also notable is that the density of cones in the synthetic mRGC cone pooling maps is higher than that seen in the macaque mRGCs. This occurs because our model is based on human cone mosaics, and human cone density is higher than macaque cone density at temporal eccentricities above 5 mm [50], which is where these comparisons are made.

To contrast the relationship in center and surround cone pooling regions between synthetic and macaque mRGCs more quantitatively we compared the diameters of cone pooling regions of the three depicted macaque mRGCs against those of populations of synthetic mRGCs at two eccentricities: 6.75 mm, and 6.0 mm. Results of this analysis are depicted in Fig. 10C1 and 10C2. The minor and major diameters of the center pooling mechanism and the diameter of the surround pooling mechanism for the 3 macaque mRGC cells are depicted by the yellow squares, pink circles and magenta stars, respectively. The corresponding distributions in populations of synthetic mRGCs are depicted by the yellow, pink and magenta histograms, respectively. Note that at 6.75 mm (Fig. 10C1), the cone pooling regions of the synthetic mRGCs are consistently larger than those of the three macaque mRGCs. However, at the slightly less peripheral eccentricity of 6.0 mm (Fig. 10C2) a better agreement exists between model and macaque mRGCs.

These observations highlight an inherent issue in building our mRGC model, namely that we had to employ a mixture of human and macaque data sources: human data regarding the density of cones and the density of mRGC RFs across visual space, human data regarding the characteristics of physiological optics across the retina, and macaque data regarding the spatial characteristics of mRGC RFs and of H1 horizontal cells, with our validations done against macaque data. This is not ideal, as there are some differences between human and macaque retinas [50]. But, it is unavoidable given the lack of complete data in either species. The modeling framework that we devised however, which incorporates data from different sources, can be easily modified as new data become available.



1183 **Fig. 10 Cone pooling maps in RF centers and surrounds: synthetic vs. macaque mRGCs**  
1184 **recorded *in vitro*.** **A:** Center and surround cone pooling weight maps for three synthetic mRGCs  
1185 at an eccentricity of 6.75 mm along the temporal raphe. Solid and dashed contours include cones  
1186 pooled by the RF center and the RF surround, respectively, with pooling weights  $> 0.005 \times$  the peak  
1187 center weight. **B:** Center and surround cone pooling weights for three macaque mRGCs recorded in  
1188 *vitro* at an eccentricity of 6.75 mm along the temporal raphe. White and black disks indicate cones  
1189 pooled by the RF center and the RF surround respectively, with same threshold pooling weights as  
1190 in A. The macaque mRGCs are from the *in vitro* recordings of Field *et al.* [15]. **C1 &C2:** Compari-  
1191 son of minor and major diameters of the center pooling mechanism (yellow squares and pink circles)  
1192 and of the surround pooling mechanism (purple stars) in the 3 macaque mRGC cells against corre-  
1193 sponding distributions (yellow, pink and magenta histograms) in populations of synthetic mRGCs at  
1194 eccentricities of 6.75 mm (C1) and 6.0 mm (C2).

1193  
1194  
1195  
1196

### 3.4 Visual *vs.* retinal space– referred RFs: the impact of physiological optics

In this section we characterize how physiological optics interacts with the retinal cone pooling within the RFs of mRGCs to shape their visual space–referred RF properties. Fig. 11 illustrates examples of this interaction at five horizontal eccentricities,  $x = [-16^\circ, -8^\circ, 0^\circ, +8^\circ, +16^\circ]$ , and 3 vertical eccentricities,  $y = [-8^\circ, 0^\circ, +8^\circ]$ . The yellow ellipses in each panel of the  $3 \times 5$  grid of Fig. 11A depict Gaussian ellipsoids fitted to the retinal space–referred RF maps of synthetic mRGCs at the examined eccentricities. The small and non-systematic orientation biases in the retinal space–referred RF maps emerge due to the pooling of multiple cones by the RF center mechanism and are reminiscent of RGC mosaics mapped *in vitro* [39].

The blue ellipses in Fig. 11B depict Gaussian ellipses fitted to the visual space–referred RF maps of the same cells. Note that there are striking and systematic orientation biases in these visual space–referred RF maps, which emerge due to the characteristics of physiological optics, whose PSFs are depicted in Fig. 11C. Clearly, the shape of the PSFs, especially at peripheral locations is a major determinant of the visual space–referred RFs in mRGCs.

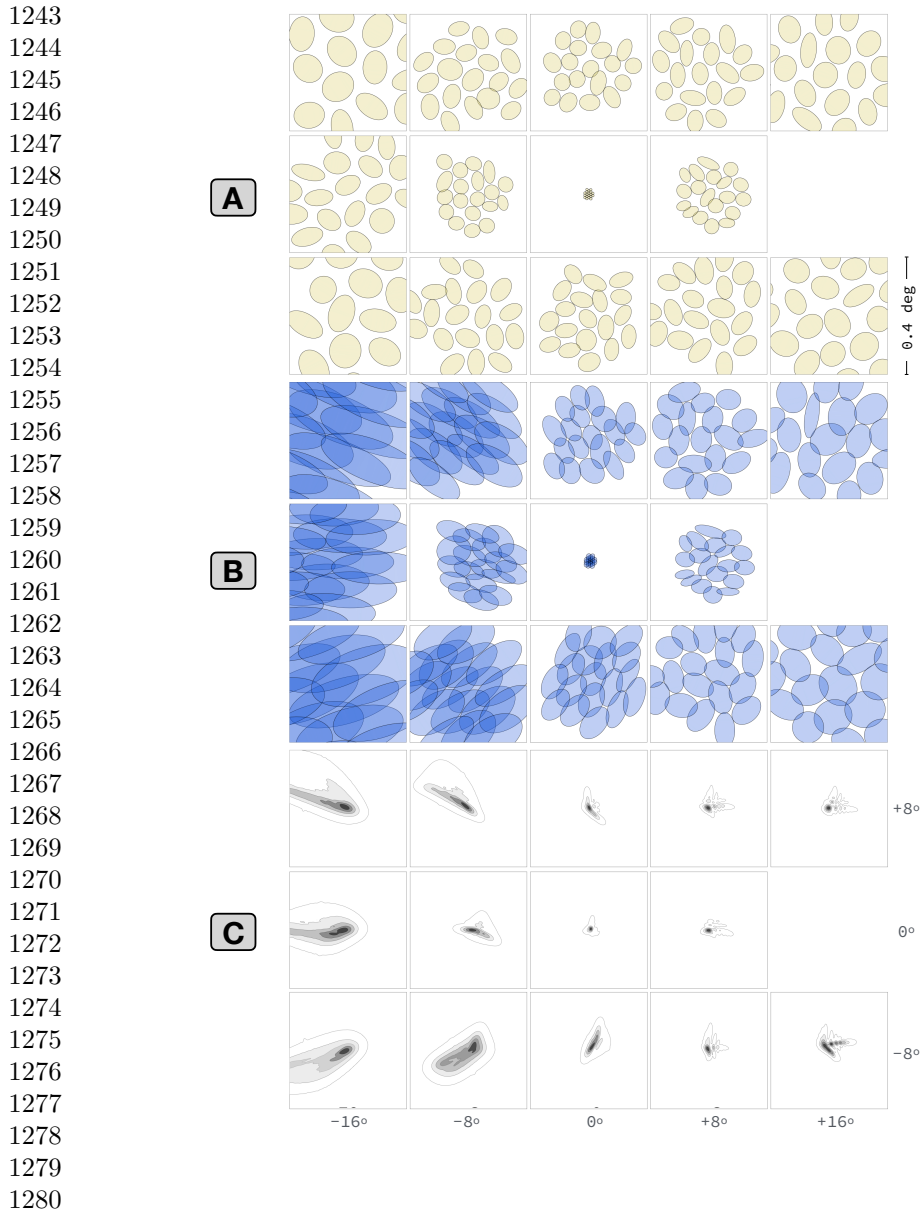
Overall, this analysis demonstrates that there can be substantial differences between *in vivo* and *in vitro* estimates of the spatial RFs of mRGCs, and, once again highlights the notion that inferences regarding retinal wiring from *in vivo* measurements must be evaluated in the context of the effect of the physiological optics. Indeed, in recent on-going work, [31], we have shown the importance of such analyses in assessing inferences regarding cone wiring to the surround subregions of mRGCs based on *in vivo* measurements of their spatio-chromatic RFs.

### 3.5 Validity of the Difference of Gaussians model applied to *in vitro* responses of mRGCs in retrieving their spatial pooling characteristics

In our synthetic mRGCs, the spatial characteristics of cone pooling within the RF center and the RF surround *component* mechanisms are known by design. This allows us to test how well one can predict these characteristics from Difference of Gaussian model fits to *in vitro* measurements of mRGC STFs, where the RF center and surround mechanisms are driven simultaneously in the absence of optics [16].

Results of this analysis are illustrated in Fig. 12. The cone pooling maps of four exemplar mRGCs are depicted in the left column. The cells in the top two rows both have RF centers with a single cone input, whereas the cell in the third row has a 2-cone RF center, and the cell in the fourth row has a 3-cone RF center.

The pink and maroon histograms depicted in the middle column of Fig. 12, are the y-axis integrated cone pooling weights within these cells’ RF center and surround sub-regions, respectively. The superimposed dashed lines depict the center and surround line weighting profiles, as estimated by the DoG model fit to the cells’ retinal space–referred STFs, which are depicted by the gray disks in the right column of Fig. 12. Note that although the DoG model fits to the computed retinal space–referred STFs (solid lines in right column) are good for all cells, the inferred spatial RF profiles, (dashed



1281 **Fig. 11 Retinal vs. visual space-referred mRGC RF maps across the retina.** Illustration  
 1282 of the effect of physiological optics on visual space-referred spatial RF maps of synthetic mRGCs  
 1283 across eccentricity. **A:** Retinal space-referred spatial RF maps at different (x,y) eccentricities. Within  
 1284 each panel, yellow contours depict Gaussian ellipsoid fits to RF maps of up to 19 cells from a single  
 1285 mRGC mosaic. RF maps are computed using white noise stimulation under diffraction limited optics.  
 1286 **B:** Visual space-referred spatial RF maps of the same cells, computed under physiological optics  
 1287 of one human subject at corresponding eccentricities. **C:** Point spread functions of the employed  
 1288 physiological optics at corresponding eccentricities.

1288

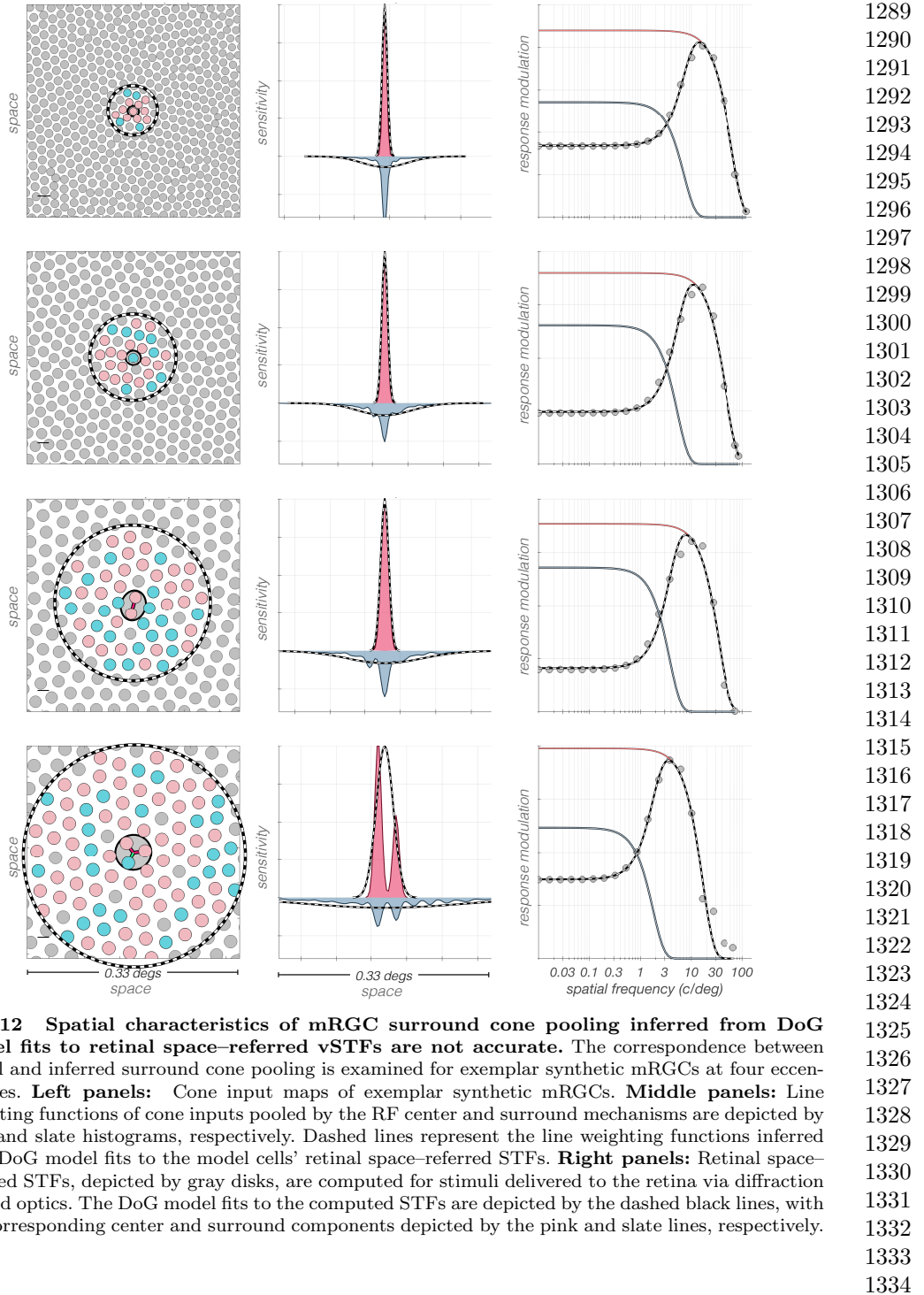


**Fig. 12** Spatial characteristics of mRGC surround cone pooling inferred from DoG model fits to retinal space-referred vSTFs are not accurate. The correspondence between actual and inferred surround cone pooling is examined for exemplar synthetic mRGCs at four eccentricities. **Left panels:** Cone input maps of exemplar synthetic mRGCs. **Middle panels:** Line weighting functions of cone inputs pooled by the RF center and surround mechanisms are depicted by pink and slate histograms, respectively. Dashed lines represent the line weighting functions inferred from DoG model fits to the model cells' retinal space-referred STFs. **Right panels:** Retinal space-referred STFs, depicted by gray disks, are computed for stimuli delivered to the retina via diffraction limited optics. The DoG model fits to the computed STFs are depicted by the dashed black lines, with the corresponding center and surround components depicted by the pink and slate lines, respectively.

1335 lines in the middle column), do not capture accurately the cone pooling regions of  
1336 the RF surrounds (slate histograms in the middle column). The discrepancy between  
1337 actual and inferred surround pooling is most obvious in the two top cells which have  
1338 single-cone RF centers, and becomes less pronounced as RF center size increases. The  
1339 discrepancy involves both the spatial extent and the peak sensitivity of the inferred  
1340 surround pooling, which is estimated by the DoG model to be more diffuse with a  
1341 weaker peak sensitivity than the cell's actual surround cone pooling.

1342 It is perhaps not surprising that the DoG model does not do a good job of fitting  
1343 the model cell surrounds, given that they were constructed as double exponentials to  
1344 match the spatial properties of H1 horizontal cells. The key point, however, is that the  
1345 DoG model fits to the observable composite STFs are quite good. These observations  
1346 suggest that caution should be exercised when inferring mRGC RF surround properties  
1347 from DoG model fits to *in vitro* STF measurements.

1348

### 1349 3.6 Applications

1350

1351 We [2, 3, 6], and others [51–53] have reported on how the representation of visual  
1352 information at the level of the cone mosaic shapes visual performance, in our case by  
1353 exploiting the ISETBio image computable model of cone excitations. The transforma-  
1354 tion from cone excitations to RGC responses further shapes the information available  
1355 for perceptual decisions, and we can interrogate our linear spatio-chromatic RF model  
1356 of the ON-center mRGC mosaic to understand how the information available from  
1357 this neuron class differs from that at the cone mosaic.

1358 In this section, we present two example computations of this nature. Our goal is to  
1359 illustrate how our model may be exploited in this way, and not to present a full analysis  
1360 in either case. Even these initial calculations, however, provide interesting insight.

1361

#### 1362 3.6.1 Achromatic and chromatic spatial contrast sensitivity

1363 We used a computational observer approach to compute spatial contrast sensitivity  
1364 functions (CSFs) for achromatic and L-M cone opponent stimuli, based both on the  
1365 representation at the cone mosaic and on the representation at the mRGC mosaic. To  
1366 do so, we computed responses to drifting gratings of varying spatial frequency,  $\omega$ .

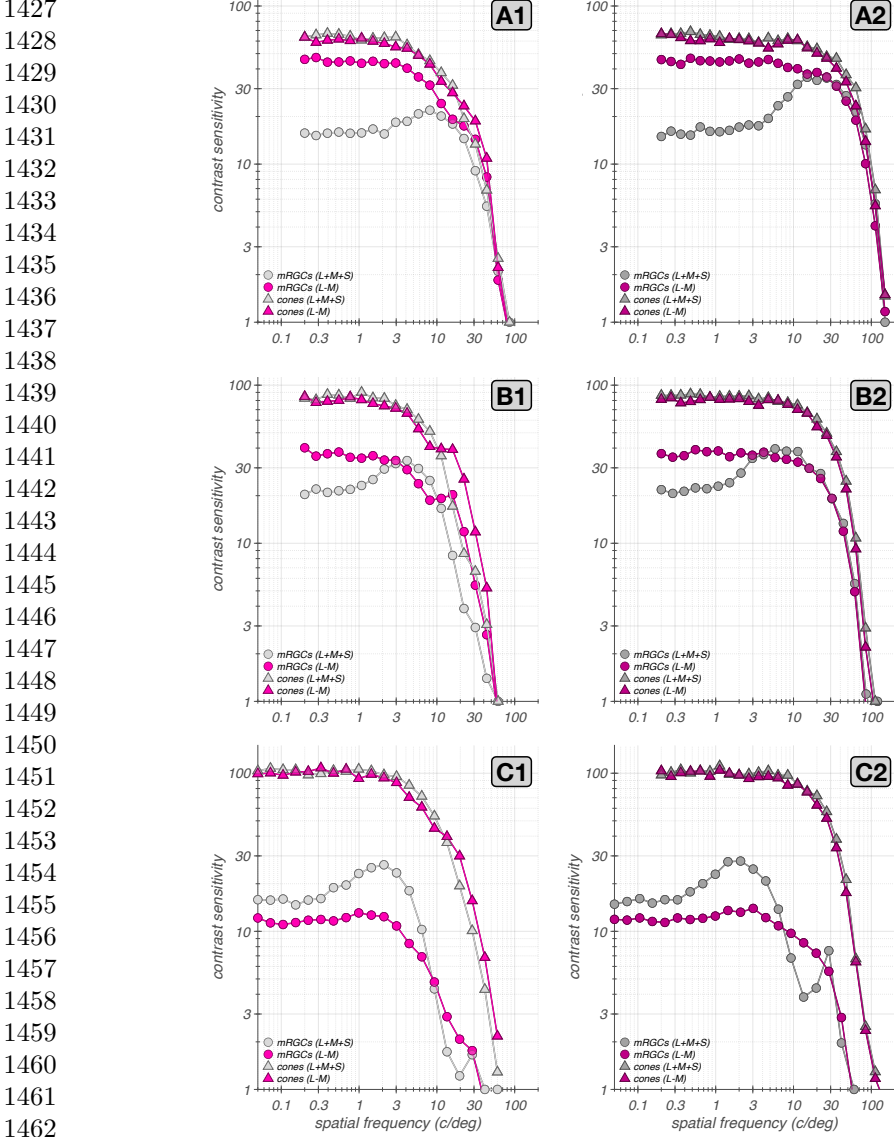
1367 For the achromatic gratings, the L-, M- and S-cone contrast component gratings  
1368 were in phase,  $C^L(\omega, x, y) = C^M(\omega, x, y) = C^S(\omega, x, y)$ . For the L – M gratings, the  
1369 L- and M-cone contrast components were in antiphase,  $C^L(\omega, x, y) = -C^M(\omega, x, y)$ ,  
1370 and  $C^S(\omega, x, y) = 0$ . For all stimuli, the mean  $(x, y)$  chromaticity was  $(0.30, 0.32)$  and  
1371 the mean luminance was  $100 \text{ cd/m}^2$ . Stimuli were simulated as presented on a typical  
1372 CRT monitor, but with 20-bit channel DACs, to avoid intrusion of quantization effects.

1373 For each eccentricity we studied, we oriented the gratings so that they were aligned  
1374 with the axis of elongation of the optical point spread function at that eccentricity.  
1375 Stimulus size was specified so that it extended over the area spanned by the input  
1376 cone mosaic of the employed mRGC mosaic. The size of the mRGC mosaics was varied  
1377 between eccentricities so as to achieve nearly equal numbers of mRGCs for mosaics  
1378 between which we wished to compare performance.

1379

1380

Cone fundamentals vary with eccentricity because of variation in macular pigment density and photopigment axial density, and this variation is captured by ISET-Bio. Therefore, in these computations, stimuli were designed using cone fundamentals specific to the eccentricity of the employed mRGC mosaic.	1381
	1382
	1383
	1384
At present, our mRGC model does not include spike generation or response noise. Therefore, in these computations we modeled response variability by adding zero mean Gaussian noise to the noise-free model mRGC responses. This approximation allows us to examine relative sensitivity across stimuli and eccentricity, but the overall level of predicted sensitivity is arbitrary. Given the choice of Gaussian noise, we used a template matching computational observer decision rule, with templates provided by the noise-free responses to the stimuli being discriminated. For comparing computational observer performance at the mRGCs with that at the cones, we also adopted the Gaussian noise approximation for the cone excitations, and used the template matching decision rule.	1385
To estimate contrast sensitivity, we varied, for each tested spatial frequency, $\omega$ , the contrast of the test stimulus and identified threshold contrast, $C_{\text{threshold}}(\omega)$ , as that for which the probability of correctly identifying the test versus a zero contrast stimulus was 80.6%. Contrast sensitivity was defined as $\text{CSF}(\omega) = 1/C_{\text{threshold}}(\omega)$ .	1386
Estimates of so computed contrast sensitivities at three eccentricities are depicted in Fig. 13. The contrast sensitivities for stimuli viewed through typical human optics are shown in the left panels of Fig. 13, with disks and triangles depicting sensitivity at the mRGC mosaic and at its input cone mosaic, respectively. For comparison, the right panels of Fig. 13 depict corresponding calculations for stimulus viewed under diffraction-limited optics with no chromatic aberration, as might be measured using adaptive optics. The comparison between left and right panels helps understand which effects in the computed CSFs have their origin in the optics or sampling by the cone mosaic, and which should be attributed to retinal processing through to the mRGCs.	1387
At the fovea, the CSFs at the cone excitation level (triangles in Fig. 13A1), are low pass for both achromatic and L-M stimuli. This is expected because there is no spatial antagonism at the level of the photopigment excitations, and because we do not incorporate spatio-temporal coupling that arises because of interactions between fixational eye movements and post-receptor temporal filtering [54, 55].	1388
On the other hand, the achromatic CSF at the mRGC mosaic exhibits a mild low-spatial frequency attenuation, which is due to the spatial antagonism between mRGC RF centers and surrounds. Note that the low frequency attenuation appears weaker than what is observed under diffraction limited optics (Fig. 13A2). This occurs because physiological optical blur carves sensitivity at the high frequency regime, thereby reducing the apparent effect of the mRGC surrounds on the CSF. We observed a similar effect in foveal macaque mRGCs whose responses were measured under adaptive optics conditions [10].	1389
The L – M opponent CSF of the mRGC mosaic lacks the low-frequency attenuation seen for achromatic modulations because in foveal mRGCs, L – M cone opponent stimuli do not induce substantial spatial antagonism between their single cone RF centers and their surrounds. These observations, which are consistent with what is known regarding the L – M chromatic contrast sensitivity of the mRGC pathway	1390
	1391
	1392
	1393
	1394
	1395
	1396
	1397
	1398
	1399
	1400
	1401
	1402
	1403
	1404
	1405
	1406
	1407
	1408
	1409
	1410
	1411
	1412
	1413
	1414
	1415
	1416
	1417
	1418
	1419
	1420
	1421
	1422
	1423
	1424
	1425
	1426



1464 **Fig. 13 Computational observer spatial CSFs.** Left column depicts CSFs computed with  
 1465 stimuli that are delivered to the retina through typical human optics. Right column depict CSFs  
 1466 computed with stimuli that are delivered to the retina under diffraction limited optics. **A1:** CSFs  
 1467 for a  $0.6^\circ \times 0.6^\circ$  foveal mRGC mosaic and of its input cone mosaic, depicted by disks and triangles,  
 1468 respectively. Gray: achromatic; pink: L-M. This mosaic contains 4628 mRGCs. **A2:** Diffraction-limited  
 1469 CSFs of the same foveal mRGC mosaic. **B1 & B2:** CSFs for a  $2.1^\circ \times 2.1^\circ$  parafoveal mRGC mosaic  
 1470 synthesized at an eccentricity of  $4^\circ$  along the temporal meridian. This mosaic contains 4633 mRGCs.  
**C1 & C2:** CSFs, respectively for a  $4.1^\circ \times 4.1^\circ$  peripheral mRGC mosaic synthesized at an eccentricity  
 1471 of  $14^\circ$  along the temporal meridian. This mosaic contains 2195 mRGCs.

1471  
 1472

[16, 56], demonstrate that L – M sensitivity exceeds achromatic sensitivity at low spatial frequencies, consistent with the literature [57].

At high spatial frequencies there is little difference between computational observer sensitivity to achromatic and L – M modulations. This is not true of human observers, where sensitivity drops more rapidly as a function of spatial frequency for red-green isoluminant gratings than for achromatic gratings either with [56] or without typical optical blur [58]. Although our L – M opponent CSFs are not precisely equivalent to the red-green isoluminant CSFs measured in many human experiments, this is not the primary source of the difference between computational and human observers. Rather, it is known that compared to ideal observers, humans lose foveal information available from the cones more rapidly as a function of spatial frequency for red-green than for achromatic gratings [53].

Our example calculation here suggests that this information loss should not be attributed to the linear receptive fields of the mRGCs. We believe this is because optical blur dominates computational observer performance at high spatial frequencies and the single cone RF centers of foveal mRGCs transmit information about each type of stimulus equally well; the surrounds have little effect at high spatial frequencies. Also, we do note that in the present calculations the specific resolution limit, i.e., the spatial frequency at which sensitivity drops to 1, depends on the variance of the added Gaussian noise and is thus somewhat arbitrary. We have chosen a noise level that is low relative to human observers so that our computations show the behavior in the high-spatial frequency regime more fully than would psychophysics conducted through natural optics.

As we move to more peripheral locations, additional features of the CSF emerge. Figs. 13B1 and 13C1 depict results of computations at 4°. Note that under physiological optics viewing (Fig. 13B1) there is a spatial frequency regime in which L – M sensitivity exceeds the corresponding achromatic sensitivity, with the L – M CSF having a notched shape. We have reported this observation in conference abstract form [59]. It occurs because of the wavelength dependent defocus that is introduced by longitudinal chromatic aberration (LCA), which can change the spatial phase of the L– and M–cone stimulus components in the retinal image. Consistent with this interpretation, the notch is present in the CSFs both at the cones and at the mRGCs on the left, but not under diffraction-limited optics (Fig. 13B2), where LCA is zero. Similar effects have been observed for S-cone CSFs [60]. We have presented in abstract form experimental results that suggest that these effects occur in measurements of the human L – M spatial CSF [61].

Comparison of the cone-based CSFs in Fig. 13A1 with those in Fig. 13B1 and Fig. 13C1 also reveals the effect of stronger optical blur with eccentricity, which increases the rolloff of the CSFs with spatial frequency. Similar comparison of the mRGC-based CSFs shows additional rolloff introduced by the increasing size of mRGC RF centers with eccentricity.

Additional observations are notable at 14° (Figs. 13C1 and 13C2). First, a notch arises in the achromatic CSF at high spatial frequencies for the mRGC CSF that is not apparent in the cone CSF. This seems unlikely to be an optical effect, because it is more salient in Fig. 13C2 where optical effects are not present. To explore the origin

1519 of this effect, we computed CSFs at different orientations (not shown), which show  
1520 that this notch is orientation dependent and has to do with the precise alignment of  
1521 individual cones with the receptive field of an mRGC. We do not explore it further  
1522 here.

1523 We also note, once again, that our computational observer is with respect to a noise  
1524 level that makes it more sensitive than the human observer, so that the notch shown  
1525 in Fig. 13C1 would be unlikely to be revealed with psychophysics conducted with  
1526 natural optics. Indeed, in further simulations (data not shown) conducted with twice  
1527 the noise variance, we observed that, in addition to an overall reduction in sensitivity,  
1528 the high frequency notch disappeared under both physiological and adaptive optics  
1529 conditions. It is an interesting question as to whether such effects could be observed  
1530 experimentally under adaptive optics conditions.

1531 Finally, note that the L – M advantage over the achromatic CSF is reversed at 14°  
1532 of eccentricity. This is because at such high eccentricities, the L – M signal is reduced  
1533 by the increased mixing of L– and M–cone signals within the larger mRGC RF centers  
1534 and surrounds. Careful comparison of this effect with computational observer predic-  
1535 tions for various choices of the model’s spatial homogeneity/spectral purity tradeoff  
1536 parameter,  $\phi$ , is an interesting future direction.

1537

### 1538 3.6.2 Chromatic contrast sensitivity of synthetic mRGC mosaics: 1539 dependence on eccentricity

1540 As a second example application, we examined chromatic sensitivity for uniform fields  
1541 modulated in different directions in the LM-cone contrast plane. We used the same  
1542 computational observer approach described above, and evaluated threshold for stimuli  
1543 whose contrast was modulated in time. The cone contrasts of stimuli at different chro-  
1544 matic directions,  $\theta$ , on the LM plane were:  $C^L(\theta) = \rho \cdot \cos(\theta)$ ;  $C^M(\theta) = \rho \cdot \sin(\theta)$ ;  $C^S(\theta) =$   
1545 0. For each  $\theta$ , we varied  $\rho$  to find its threshold value for discriminating that modula-  
1546 tion direction from a zero contrast stimulus with a probability of 0.806. To summarize  
1547 the computed thresholds across the different chromatic directions, we fit ellipses to  
1548 the locus of threshold contrast points.

1549 Fig. 14 depicts computational observer thresholds for synthetic mRGC mosaics and  
1550 for their input cone mosaics at different eccentricities. Note that how computational  
1551 observer sensitivity changes with eccentricity depends on how stimulus size is covaried  
1552 with eccentricity, as does human sensitivity (e.g. [62]). Comparison of the magnitude  
1553 of sensitivity for cone- and mRGC-based computational observers depends on how the  
1554 noise levels are chosen. For these example calculations, we focus on the shape rather  
1555 than magnitude of the elliptical threshold contours. Therefore, each contour shown in  
1556 Fig. 14 is normalized so that the threshold along the M cone direction is equal to one.

1557 A few observations are notable. First, the normalized contours for the cone-based  
1558 observer are similar across eccentricities and align with the L– and M–cone contrast  
1559 axes. They are more elongated in the M–cone direction because our mosaics have more  
1560 L cones than M cones. The alignment with the axes is expected [63], and the similarity  
1561 of the normalized shapes occurs because this shape depends primarily on the relative  
1562 numbers of L and M cones.

1563

1564

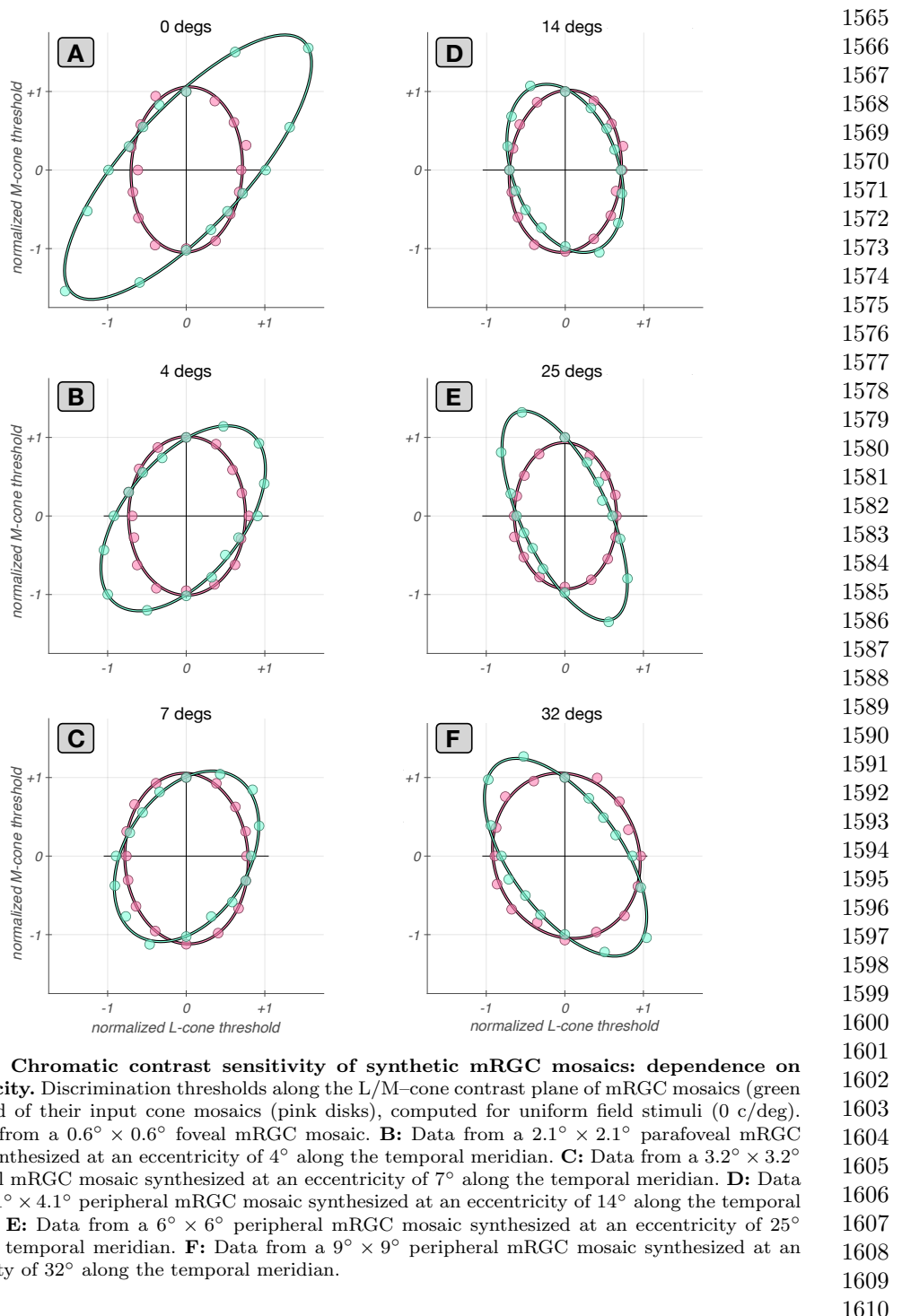


**Fig. 14 Chromatic contrast sensitivity of synthetic mRGC mosaics: dependence on eccentricity.** Discrimination thresholds along the L/M-cone contrast plane of mRGC mosaics (green disks) and of their input cone mosaics (pink disks), computed for uniform field stimuli (0 c/deg). **A:** Data from a  $0.6^\circ \times 0.6^\circ$  foveal mRGC mosaic. **B:** Data from a  $2.1^\circ \times 2.1^\circ$  parafoveal mRGC mosaic synthesized at an eccentricity of  $4^\circ$  along the temporal meridian. **C:** Data from a  $3.2^\circ \times 3.2^\circ$  parafoveal mRGC mosaic synthesized at an eccentricity of  $7^\circ$  along the temporal meridian. **D:** Data from a  $4.1^\circ \times 4.1^\circ$  peripheral mRGC mosaic synthesized at an eccentricity of  $14^\circ$  along the temporal meridian. **E:** Data from a  $6^\circ \times 6^\circ$  peripheral mRGC mosaic synthesized at an eccentricity of  $25^\circ$  along the temporal meridian. **F:** Data from a  $9^\circ \times 9^\circ$  peripheral mRGC mosaic synthesized at an eccentricity of  $32^\circ$  along the temporal meridian.

1611 Second, in contrast, the mRGC-based threshold contours change markedly with  
1612 eccentricity. For the foveal mosaic, the threshold ellipse is highly elongated along  $45^\circ$   
1613 in the L/M-cone contrast plane, indicating that the highest discrimination thresholds  
1614 occur when  $c^L = c^M$  and lowest thresholds occur when  $c^L = -c^M$ . This difference  
1615 in comparison to the cone-based computations is a consequence of the chromaticic-  
1616 opponency of foveal mRGC RFs, which have single cone centers, and thus opponency  
1617 between their centers and the surrounds as the surrounds draw on mixed cone-types  
1618 [64, 65]. This opponency leads to cancellation of non-opponent L- and M-cone signals  
1619 for low spatial frequency stimuli and thus the observed contour elongation along  $45^\circ$   
1620 [63, 66].

1621 Third, as eccentricity increases, the contours first become less elongated and then  
1622 elongation starts increasing again but along the  $135^\circ$  rather than the  $45^\circ$  axis. This  
1623 is because the cone non-selective wiring model we implemented leads to progressively  
1624 less opponency with increasing RF center size [16, 64, 65].

1625 Although the qualitative features that emerge from this example calculation are  
1626 understood in the literature, the example illustrates that our model enables this type  
1627 of calculation to be made quantitatively in a way that takes chromatic aberration,  
1628 stimulus size and spatial frequency and retinal position into account. Of particular  
1629 interest to us will be exploring how this type of threshold contour varies with the the  
1630 tradeoff between spatial homogeneity and spectral purity of mRGC RF centers (the  
1631 center wiring parameter  $\phi$  of our model).

1632

## 1633 4 Discussion

1634

1635 We developed an image computable model of the linear spatio-chromatic RF mosaic  
1636 of mRGCs across the retina. The model extends our image-computable cone mosaic  
1637 model [2, 3] by adding a layer of mRGCs which pool signals directly from the cone  
1638 mosaic. The connectivity between cones and mRGCs is derived using a simulation  
1639 framework that integrates anatomical, physiological and optical quality data, all of  
1640 which vary across eccentricity.

1641 By explicitly modeling the optics and photoreceptors, rather than directly express-  
1642 ing the RFs in terms of the stimulus, we are able to link our model with both *in-vitro*  
1643 and *in-vivo* data, and to make predictions over a range of experimental conditions  
1644 that are otherwise difficult to compare. These include psychophysical and physiolog-  
1645 ical measurements made through physiological optics (natural viewing conditions),  
1646 interferometric and adaptive optics techniques that bypass or correct for optical  
1647 aberrations, and *in-vitro* physiology, where the natural optics are not present.

1648 To build the model we had to overcome the challenge that current data about  
1649 mRGC properties are incomplete and, where they exist, may come from different  
1650 species, different measurement modalities, and from different eccentricities. For exam-  
1651 ple, there are *in-vivo* measurements of mRGC linear receptive fields across the retina  
1652 [17], but physiological optics blur the stimuli so that they do not constrain mRGC  
1653 input at the cone-by-cone resolution we seek. On the other hand, although there is  
1654 single cone-resolution connectivity data from *in-vitro* physiology [15], these data are  
1655  
1656

currently limited to large eccentricities ( $\geq 25^\circ$ ). Thus, we developed a modeling framework that allows integration of data from multiple sources. This framework is an important contribution in its own right; we expect it will be useful to us and others, for incorporating new data that become available and for modeling other RGC classes.	1657
	1658
	1659
	1660
	1661
We showed that the model captures visual space-referred spatial RF properties of macaque mRGCs recorded <i>in-vivo</i> across eccentricities, as well as retinal space-referred spatial RF properties of macaque mRGCs recorded <i>in-vitro</i> . We also showed that physiological optics plays a major role in shaping the visual space-referred spatial RF properties, so that inferences regarding retinal circuitry made from <i>in-vivo</i> measurements need to be evaluated in the context of the optics. Further, we showed that even under <i>in-vitro</i> conditions, where the optics are eliminated, the traditional approach of fitting a Difference of Gaussian model to spatial responses can lead to incorrect assessments of the properties of cone pooling in the mRGC surrounds.	1662
	1663
	1664
	1665
	1666
	1667
	1668
	1669
	1670
	1671
	1672
	1673
	1674
	1675
	1676
	1677
	1678
	1679
	1680
	1681
	1682
	1683
	1684
	1685
	1686
	1687
	1688
	1689
	1690
	1691
	1692
	1693
	1694
	1695
	1696
	1697
	1698
	1699
	1700
	1701
	1702

1703 not been our goal, we would have had to bring in human data to characterize the  
1704 physiological optics across the visual field, as such data are not currently available in  
1705 macaque. At the same time, not all the required data are available for human: although  
1706 measurements of cone and mRGC density and physiological optics across the retina  
1707 are available, physiological characterizations come from the macaque.

1708 The need to mix data across the two closely related species produces tension in  
1709 cases where the parameters for the two species differ. An example is the different  
1710 cone densities in the far periphery [50], which intrudes on the interpretation of the  
1711 comparison between our model and *in-vitro* physiology in that retinal region. As more  
1712 data become available in both species, and as species differences come more fully into  
1713 focus [67], our approach should allow more fully differentiated models to be developed  
1714 targeted at each.

1715

#### 1716 4.2.2 Noise, nonlinearities and temporal dynamics

1717 Although the current model captures fundamental aspects of the visual representation  
1718 at the level of the mosaic of ON mRGCs, there are known characteristics of mRGCs  
1719 that it does not account for. These include static and spatial nonlinearities, temporal  
1720 filtering, spike generation, and physiologically constrained response noise. The modeling  
1721 framework we developed is extensible however, so that these components may be  
1722 included through future work.

1723 Response variability models are available for macaque mRGCs, as descriptions of  
1724 spike generation mechanisms [26, 33, 68]. In addition, we can incorporate nonlinearities,  
1725 such as (a) adaptation effects introduced through the phototransduction cascade  
1726 [69], (b) compressive and expansive static nonlinearities in the output of mRGCs  
1727 [23, 33], and (c) spatial nonlinearities introduced by rectifying sub-units within the  
1728 RFs of mRGCs [21, 22]. Explicit inclusion of photocurrent-based responses in the  
1729 input to the mRGCs introduces a temporal component to the response model [69]. In  
1730 addition, a second temporal filter may be added, such that when combined with the  
1731 photocurrent filter will yield the bandpass filter characteristics observed in macaque  
1732 mRGCs [25].

1733 Our current model does not represent explicitly the properties of the retinal circuitry (horizontal, bipolar, and amacrine cells) that produces the mRGC response  
1734 properties, as we have opted instead to work towards a functional model that describes  
1735 those properties. A complementary mRGC modeling approach that does consider some  
1736 of these cell types explicitly has recently been published [30], and there are other  
1737 modeling efforts that have examined the influence of the various retinal interneurons  
1738 on RGC response properties [28, 32]. We note however, that some of the processing  
1739 performed by these other retinal cell types is incorporated implicitly in the current  
1740 cone-to-mRGC model, such as the parametric form of the surrounds inherited from  
1741 H1 cells.

1742 The framework we developed is designed so that it would be possible to interpose  
1743 explicit models of intermediate retinal cell types. Representing the action of different  
1744 cell types explicitly may in the longer run be an effective way to account for response  
1745 nonlinearities in the mRGCs, or in other classes of retinal ganglion cells. Moreover,  
1746 using our framework to model other cell classes may be of interest to those seeking to

interpret responses of those classes *per se*, or in the retinal mechanisms that produce RGC response properties. 1749  
1750  
1751

#### 4.2.3 OFF mRGC mosaic

Because we model the linear RF, the distinction between ON and OFF mRGCs is subtle. However, our model should be thought of as a model of only the ON mRGCs because the synthetic cells only pool signals from L- and M-cones. This is believed true for ON mRGCs, but recent evidence suggests that OFF mRGCs draw upon all three types of cones in their RF centers [15, 37, 38]. Incorporating S-cone input into an OFF-center mRGC model is straightforward.

Another question that arises when considering a model of OFF mRGC mosaic is how to split the density of mRGCs in two populations at different eccentricities. In the current model, the ON mRGC density was assumed to be half of all mRGCs across all eccentricities. This seems reasonable for central retina where mRGC centers draw primarily on a single cone and where anatomical evidence suggests that each cone provides input to the center of one ON and one OFF midget bipolar cell. However, there is evidence that the RFs of peripheral ON midget (and parasol) RGCs are larger than their OFF counterparts in both human and macaque retinas [40]. This implies that the density of ON RGC cells might be lower in the periphery than that of OFF cells, given that ON and OFF mRGCs have similar RF overlap [39]. One idea is to treat the asymmetry between ON and OFF mRGC RF densities in an eccentricity-dependent manner, similar to the way we encoded a variable-with-eccentricity RF center overlap.

Finally, when adding an OFF mRGC mosaic one should allow for the possibility of coordination between the ON and the OFF submosaics, to account for recent observations regarding systematic shifts in the spatial layouts of ON and OFF mRGCs [70].

### Using the software

The developed software for synthesizing ON mRGCm mosaics across the retina and for computing with them is part of ISETbio and is freely available at

<https://github.com/isetbio/isetbio>. An introduction to using the mRGCmosaic software is available at:

[https://github.com/isetbio/isetbio/wiki/Retinal-ganglion-cell-\(RGC\)-mosaics](https://github.com/isetbio/isetbio/wiki/Retinal-ganglion-cell-(RGC)-mosaics), and a number of MATLAB tutorials specific to the mRGCmosaic can be found at <https://github.com/isetbio/isetbio/tree/main/tutorials/mrgc>.

These tutorials demonstrate (a) how to use mosaics of ON mRGCs that have been synthesized at a number of eccentricities, and (b) how to build and validate mRGC mosaics at any desired eccentricity, using a number of design choices. A summary of current available tutorials is shown in Table 1.

**Acknowledgements.** We thank Lisa Croner and the late Ehud Kaplan for help with procedures followed during collection of the macaque *in vivo* data, Greg Field for providing insight on details regarding *in vitro* macaque data, and E. J. Chichilnisky, Tyler Godat, David Williams, and Fangfang Hong for helpful discussions.

1795 **Table 1 List of tutorials for computing with mRGC mosaics and de novo**  
 1796 **synthesis of mRGC mosaics.**

1797	<b>Tutorial name</b>	<b>Scope</b>
<i>Computing with mRGC mosaics</i>		
1799	<code>t_mRGCMosaicVisualizeWithOptics.m</code>	Visualizes a previously synthesized mRGC mosaic and the optics that were used for its synthesis
<i>Synthesizing mRGC mosaics</i>		
1800	<code>t_mRGCMosaicSynthesizeAtStage1.m</code>	Denovo synthesis of the spatial position lattices of cones and mRGC RF centers (stage 1)
1801	<code>t_mRGCMosaicSynthesizeAtStage2.m</code>	Denovo synthesis of an mRGC mosaic at different sub-stages of cone-to-mRGC RF center connectivity (stage 2)
1802	<code>t_mRGCMosaicSynthesizeAtStage3.m</code>	Denovo synthesis of an mRGC mosaic at different sub-stages of cone-to-mRGC RF surround connectivity (stage 3)
1803		
1804		
1805		
1806		
1807		
1808		
1809		
1810		
1811		
1812		
1813		
1814		

1815  
 1816  
**1817 Declarations**

1819  
**1820 Funding**

1821 This work was supported by Facebook Reality Labs and by the Air Force Office of  
 1822 Scientific Research (FA-9550-22-1-0167 and FA-9550-22-1-0044).  
 1823

1824 **Conflict of interest/Competing interests**

1825 Not applicable

1827

1828 **Ethics approval and consent to participate**

1829 Not applicable

1830 Not applicable

1831

1832 **Consent for publication**

1833 Not applicable

1834

1835 **Data availability**

1836 Datasets (mRGCmosaics) generated during the current study are available at:

1837 [1838 https://github.com/isetbio/isetbio/tree/main](https://github.com/isetbio/isetbio/tree/main)

1839

1840

<b>Materials availability</b>	1841
Not applicable	1842
	1843
<b>Code availability</b>	1844
The code used to generate the data, and various tutorials on how to use the software are available at: <a href="https://github.com/isetbio/isetbio/tree/main">https://github.com/isetbio/isetbio/tree/main</a>	1846
	1847
	1848
An introduction to using the software is available at:	1849
<a href="https://github.com/isetbio/isetbio/wiki/Retinal-ganglion-cell-(RGC)-mosaics">https://github.com/isetbio/isetbio/wiki/Retinal-ganglion-cell-(RGC)-mosaics</a>	1850
	1851
	1852
<b>Author contribution</b>	1853
NPC: conceptualization, algorithm development, coding, data curation, validation, visualization, writing of original draft	1855
DHB: conceptualization, coding, reviewing and editing of manuscript	1856
BW: conceptualization, coding, reviewing and editing of manuscript	1857
	1858
	1859
	1860
	1861
	1862
	1863
	1864
	1865
	1866
	1867
	1868
	1869
	1870
	1871
	1872
	1873
	1874
	1875
	1876
	1877
	1878
	1879
	1880
	1881
	1882
	1883
	1884
	1885
	1886

1887 **Appendix A Deriving cone weights to the mRGC  
1888 RF centers**  
1889

1890 **A.1 Local topology-based convergent connections (stage 2A)**  
1891

1892 During the first sub-stage of cone-mRGC RF center connectivity, cones are connected  
1893 to single mRGC RF centers based on the local topology of the 2 lattices. Starting with  
1894 the cell whose RF center is at most central location of the mRGC lattice, we connect  
1895  $n_{pool}(\epsilon)$  number of L– and M–cones to it,

1896  
1897 
$$n_{pool}(\epsilon) = \lfloor \frac{D_{cones}(\epsilon)}{D_{mRGCRF}(\epsilon)} \rfloor \quad (A1)$$
  
1898

1899 where  $D_{cones}(\epsilon)$  and  $D_{mRGCRF}(\epsilon)$  are the local spatial densities of the cone mosaic  
1900 and of the mRGC RF centers, respectively, at the eccentricity,  $\epsilon$ , of the target mRGC.  
1901

1902 We draw from the nearest  $n_{pool}(\epsilon)$ , typically 6, cones that have not yet been con-  
1903 nected and whose distance to the mRGC RF center does not exceed a fraction of the  
1904 local mRGC RF center spacing. This fraction is a parameter of the model and for the  
1905 work presented here was set to 0.6.

1906 Continuing with these assignments of cones to mRGC RF centers, we move outward  
1907 to more peripheral locations in the mRGC RF mosaic, connecting cones to each mRGC  
1908 center. Any L– and M–cones that remain unconnected at the end of this sub-stage are  
1909 then connected to their nearest mRGC center, so that all cones are connected to one  
1910 mRGC center.

1911 This sub-stage can result in local inhomogeneities in both the number of cones and  
1912 the type of cones pooled within neighboring RF centers. These inhomogeneities are  
1913 smoothed out as part of the next sub-stage.

1914  
1915 **A.2 Optimizing cone connections to mRGC RF centers  
1916 (stage 2B)**

1917 In the second sub-stage of the RF center connectivity, convergent connections from  
1918 multiple cones to single mRGC RF centers are optimized according to a desired balance  
1919 between spatial and spectral inhomogeneities. This is achieved by reassigning cones  
1920 between nearby mRGC RF centers, which itself occurs in two steps.  
1921

1922 In the first step, we allow cone reassessments to a target mRGC from neighboring  
1923 mRGCs that have a higher input cone numerosity in their RF centers. In the second  
1924 step, we allow cone swaps between a target mRGC and its neighbors, independently  
1925 of their input cone numerosities.

1926 The heuristics followed in the first step are as follows. We begin by targeting  
1927 mRGCs with a single input cone and continue to target mRGCs with progressively  
1928 higher input cone numerosity. Within each set of targeted input cone numerosity,  
1929 mRGCs are sorted based on ascending retinal eccentricity. For each targeted mRGC  
1930 we determine up to 6 neighboring mRGCs which have input numerosity that exceeds  
1931 that of the target mRGC by at least 2 cones.  
1932

Cone reassessments from the candidate donor mRGCs to the target mRGC are executed in multiple passes. Starting with the neighboring mRGC of the highest input numerosity, we determine the best transfer of a single cone. If there are no eligible donor nearby mRGCs, we move to the next targeted mRGC. If there is a single candidate, we accept it and execute the cone transfer. If there are more than one candidates, for each candidate donor mRGC (up to 6) we compute a cost function, C, for reassigning each of its cones to the target mRGC, and pick the transfer that minimizes C across all cones and all candidate donor mRGCs. The cost function is described in more detail below.

Once the optimal cone transfers for each mRGC of the targeted input cone numerosity are executed, we move to the next pass, examining possible transfers from neighboring mRGCs of one lower input cone numerosity than before, but still higher than the input cone numerosity of the targeted mRGCs. Once all passes are executed, this process is repeated, now targeting mRGCs with increasing input cone numerosity, until all input cone numerosities have been targeted.

In the second step, we only allow for cone swaps between an mRGC RF center and one of its neighbors. For each mRGC of the targeted input cone numerosity, we determine its 6 closest neighbors, but now without regard to their input cone numerosity. For each of these neighboring mRGCs, we evaluate the cost function, C, for all possible combinations of cones from the target mRGC and cones from the neighboring mRGC and pick the combination that minimizes C. The selected cone swap is executed only if the post-swap value of C is lower than its pre-swap value. Multiple passes through the entire mRGC mosaic, are executed, with each pass targeting mRGCs with progressively higher input cone numerosity.

The cost function, C, employed to determine the optimal transfer/swapping is based on the position and types of the cones pooled by the target mRGC,  $t$ , and the examined neighboring mRGC,  $t_i$ . For each examined pair of mRGCs,  $(t, t_i)$ ,  $C^{(t, t_i)}$  is defined as:

$$C^{(t, t_i)} = \phi \cdot C_{\chi}^{(t, t_i)} + (1 - \phi) \cdot C_{\lambda}^{(t, t_i)} \quad (\text{A2})$$

where  $C_{\chi}^{(t, t_i)}$  is a spatial compactness cost component,  $C_{\lambda}^{(t, t_i)}$  is a spectral purity cost component, and  $\phi$  is a free parameter that controls the desired trade-off between spatial compactness and spectral purity of the RF centers.

The spatial compactness cost component,  $C_{\chi}^{(t, t_i)}$ , is defined as:

$$C_{\chi}^{(t, t_i)} = C_{\chi_N}^{(t, t_i)} + C_{\chi_o}^{(t, t_i)} \quad (\text{A3})$$

In Eq. A3,  $C_{\chi_N}^{(t, t_i)}$  quantifies the differential input cone numerosity between the examined pair of mRGCs, and is defined as:

$$C_{\chi_N}^{(t, t_i)} = |(N_L^t + N_M^t) - (N_L^{t_i} + N_M^{t_i})| \quad (\text{A4})$$

with  $N_L^t$  and  $N_M^t$  are the numbers of L- and M-cones pooled by the RF center of mRGC  $t$ , respectively.

1979 The  $C_{\chi_o}^{(t,t_i)}$  component of Eq. A3 is a spatial overlap cost component, defined as  
1980 the inverse of the distance between the centroids,  $(P^t, P^{t_i})$ , of the cones pooled by the  
1981 two mRGCs, normalized by the sum of their spatial standard deviations,  $(\sigma^t, \sigma^{t_i})$ :

1982

$$1983 C_{\chi_o}^{(t,t_i)} = 1 / \left( \frac{\|P^t - P^{t_i}\|}{\sigma^t + \sigma^{t_i}} \right) \quad (A5)$$

1985

1986 A low value of  $C_{\chi_o}^{(t,t_i)}$  indicates low overlap between the sets of cones pooled by the  
1987 examined pair of mRGCs and conversely, a high value indicates a large overlap.

1988 The  $C_{\lambda}^{t,t_i}$  term, in Eq. A2, is a cost component quantifying the sum of spectral  
1989 impurities of the pair of analyzed mRGCs:

1990

$$1991 C_{\lambda}^{t,t_i} = C_{\lambda}^t + C_{\lambda}^{t_i} \quad (A6)$$

1992

1993 The spectral impurity,  $C_{\lambda}^t$ , quantifies the degree of non-specificity, with regard to the  
1994 type of cone, in the pooling withing the RF center of an mRGC, and is defined as:

1995

$$1996 C_{\lambda}^t = \frac{\min([N_L^t, N_M^t])}{N_L^t + N_M^t} \quad (A7)$$

1998

1999 Values of  $C_{\lambda}^t$  near zero indicate a low amount of mixture of L- and M-cones, and  
2000 therefore a RF with a high degree of spectral purity, and conversely, values of  $C_{\lambda}^t$ , near  
2001 0.5, indicate an equal mixture of L- and M-cones, and therefore a RF center with a  
2002 low degree of spectral purity.

2003 The tradeoff parameter  $\phi$  factor in Eq. A2, controls how the optimal cone trans-  
2004 fer/swap is determined. When  $\phi = 1$ , cone reassessments/swaps are selected so as  
2005 to minimize the spatial compactness cost, when  $\phi = 0$ , cone reassessments are cho-  
2006 sen so as to minimize the spectral purity cost, and for intermediate values of  $\phi$ , cone  
2007 reassessments are chosen so as to minimize a ratio of the two costs.

2008

### 2009 A.3 Divergent cone connections to multiple mRGC RF 2010 centers (stage 2C)

2011

2012 In the final sub-stage of establishing the RF center connectivity, the exclusivity of  
2013 connections is relaxed, and cone connections are allowed to diverge to more than one  
2014 mRGC RF center. This divergence is guided by *in-vitro* measurements of mRGC RF  
2015 center overlap in the macaque [39].

2016 According to these observations, neighboring mRGC RF centers abut at approxi-  
2017 mately one standard deviation of their Gaussian RF profile. One caveat of using these  
2018 *in-vitro* measurements to establish cone divergence in the model, is that these measure-  
2019 ments are only available in the far periphery (30–40 degrees), with no data available  
2020 for more central locations. Anatomical studies suggest, however, that, in the central  
2021 retina, there must be little to no divergence of cone signals to mRGCs RF centers, so  
2022 we chose to implement an eccentricity-varying divergence in our model.

2023 We begin by fitting an ellipsoid to the spatial pooling map of cones that are exclu-  
2024 sively connected to the RF center of an mRGC, and extracting the rotation,  $\alpha$ , and

the major/minor axes,  $\sigma_x, \sigma_y$  of the fitted ellipsoid. Next, a super-Gaussian ellipsoid,  $G(x, y, n)$ , defined as:

$$G(x, y, n) = \exp \left[ -0.5 \times \left( \sqrt{(y'^2 + y'^2)} \right)^n \right] \quad (A8)$$

where:

$$\begin{bmatrix} x' & y' \end{bmatrix} = \begin{bmatrix} x & y \end{bmatrix} \cdot \begin{bmatrix} \cos(\alpha) & -\sin(\alpha) \\ \sin(\alpha) & \cos(\alpha) \end{bmatrix} \cdot \begin{bmatrix} 1/\sigma_x & 0 \\ 0 & 1/\sigma_y \end{bmatrix} \quad (A9)$$

is computed by scaling the values of  $\sigma_x, \sigma_y$  by a common factor, so that the value of  $G(x, y, n)$ , evaluated at the most remote exclusively-connected cone(s) is  $k \times e^{-1/2}$ . The value of  $k$  is determined empirically so that RF maps of nearby mRGCs computed under diffraction-limited optics abut when their sensitivities drop to  $e^{-1/2}$  (per [39]).

By varying the exponent of the super Gaussian,  $n$ , we model varying degrees of cone divergence. When  $n = 10$ , we obtain a flat-top Gaussian with very sharp fall-offs, modeling minimal cone divergence. When  $n = 2$ , we get a standard Gaussian modeling cone divergence that is consistent with the *in-vitro* measurements of RF center overlap at peripheral locations.

By varying  $n$  with eccentricity using a sigmoidal function we obtain a gradual transition in cone divergence with eccentricity. The slope and mid-point of the sigmoidal variation of  $n$  are currently chosen arbitrarily, with the only restrictions that above  $15^\circ$ ,  $n$  is stable at 2.0, and below  $7^\circ$ ,  $n$  is stable at 10.0. The weights of divergent cone-mRGC RF center connections are computed by evaluating the super-Gaussian ellipsoid at the positions of all cones in the vicinity of the examined mRGC.

## Appendix B Deriving cone weights to the mRGC RF surrounds

### B.1 Choosing physiology-based constraints for deriving surround cone weights in stage 3B

The optimization of the parameters of the surround cone pooling functions at each iteration is driven by the residual between the visual STF that is computed based on the surround pooling weights at the previous iteration and the Difference of Gaussians model fit to it,  $DOG(\omega)$ , which is given by:

$$DOG(\omega) = K_c \cdot R_c^2 \cdot \exp[-\pi \cdot R_c \cdot \omega]^2 - K_s \cdot R_s^2 \cdot \exp[-\pi \cdot R_s \cdot \omega]^2 \quad (B10)$$

This aspect of the optimization captures the observation that DoG models provide a reasonable fit to *in-vivo* mRGC RFs. To ensure adherence to the *in-vivo* data of Croner & Kaplan, the  $DOG(\omega)$  model fit is constrained so that the ratio of surround to center radii,  $R_s/R_c$ , and the ratio of surround to center integrated sensitivities,  $K_s/K_c \times (R_s/R_c)^2$ , both remain within a specified tolerance value,  $\tau = 0.15$ , from the mean values of the corresponding ratios for the Croner & Kaplan population of macaque mRGCs at the eccentricity of the synthesized mRGC.

2071 Specifically, for the model's  $R_s/R_c$  ratio, we enforce  
2072

$$\frac{R_s^m}{R_c^m} \times (1 - \tau) \leq \frac{R_s}{R_c} \leq (1 + \tau) \times \frac{R_s^m}{R_c^m} \quad (\text{B11})$$

2075  
2076 where  $R_c^m$  and  $R_s^m$  are the mean values of center and surround radii across the Croner  
2077 & Kaplan population of macaque mRGCs at the eccentricity of the synthesized mRGC.  
2078 The model's  $K_s/K_c \times (R_s/R_c)^2$  ratio is constrained in the same way.

2079 The residual between the visual STF and the Difference of Gaussians model fit to  
2080 it, drives the optimization of the surround pooling function. This function is a double  
2081 exponent (following the H1 horizontal cell spatial RF in the macaque [43]):  
2082

$$\mathbf{W}_s(r) = K_{\text{wide}} \times \exp[-r/R_{\text{wide}}] + K_{\text{narrow}} \times \exp[-r/R_{\text{narrow}}] \quad (\text{B12})$$

2084  
2085 To ensure that the surround pooling function remains consistent with parameter  
2086 values observed in macaque H1 cell [43], the optimization of  $\mathbf{W}_s(r)$  is constrained  
2087 so that ratio of radii,  $R_{\text{narrow}}/R_{\text{wide}}$ , and the ratio of volumes,  $V_{\text{narrow}}/V_{\text{wide}} =$   
2088  $K_{\text{narrow}}/K_{\text{wide}} \times (R_{\text{narrow}}/R_{\text{wide}})^2$ , of the two exponentials both remain within a  
2089 specified tolerance range of the macaque data.

2090 In the present work, the tolerance range for  $R_{\text{narrow}}/R_{\text{wide}}$  was set to [0.07, 0.35]  
2091 for all mosaics, whereas the tolerance range for  $V_{\text{narrow}}/V_{\text{wide}}$  was set to [0.01, 0.6]  
2092 for mosaics at eccentricities  $\leq 15^\circ$ , to [0.3, 0.9] for eccentricities in  $15^\circ \dots 25^\circ$ , and to  
2093 [0.6, 1.3], for eccentricities  $\geq 25^\circ$ .

2094 The joint manipulation of the tolerance values applied to the parameters of the  
2095 DOG model fit to the vSTF, and to the parameters of the double exponential surround  
2096 pooling model,  $\mathbf{W}_s(r)$ , allows for different options for deriving spatial pooling functions  
2097 in synthetic mRGC surrounds.

2098 One option is to set very strict tolerances on the parameters of DoG model fit to  
2099 the achieved vSTF, while allowing for a large tolerance in the parameters of  $\mathbf{W}_s(r)$ .  
2100 Results of this choice are depicted in the left-most column of Figure B1. A second  
2101 option would be to allow medium tolerance levels in both the DoG model fit and  
2102 the  $\mathbf{W}_s(r)$ . Results of this choice are depicted in the middle column of Figure B1.  
2103 A third option would be to enforce strict tolerances in  $\mathbf{W}_s(r)$ , for example matching  
2104 parameters of individual H1 horizontal cells, while allowing for a loose tolerance in the  
2105 DoG model fit. Results of this choice are depicted in the right column of Figure B1.  
2106 In the present work, we chose the second option.

2107  
2108  
2109  
2110  
2111  
2112  
2113  
2114  
2115  
2116

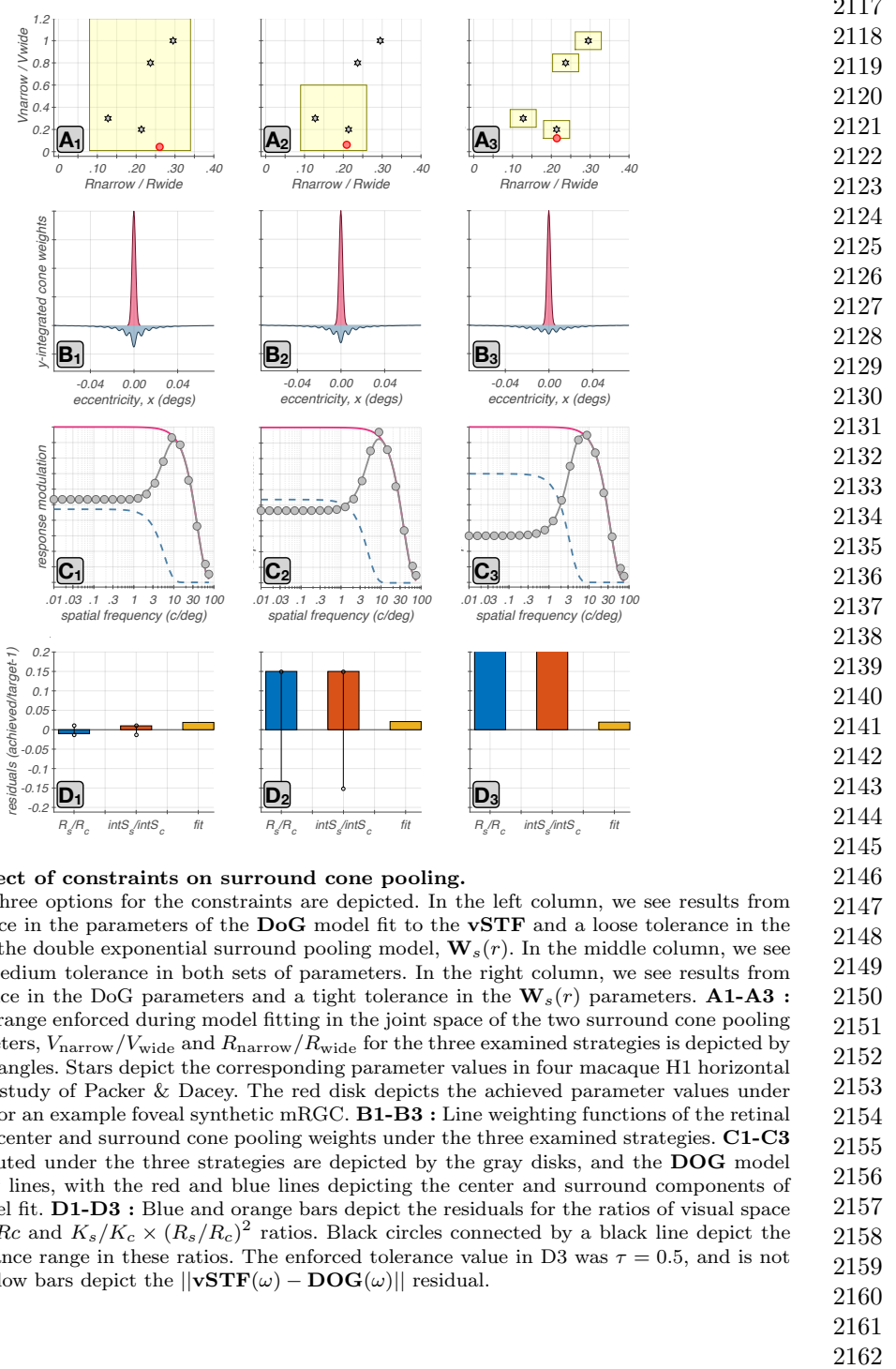


**Fig. B1 Effect of constraints on surround cone pooling.**

Results from three options for the constraints are depicted. In the left column, we see results from a tight tolerance in the parameters of the DoG model fit to the vSTF and a loose tolerance in the parameters of the double exponential surround pooling model,  $\mathbf{W}_s(r)$ . In the middle column, we see results from medium tolerance in both sets of parameters. In the right column, we see results from a loose tolerance in the DoG parameters and a tight tolerance in the  $\mathbf{W}_s(r)$  parameters. **A1-A3** : The tolerance range enforced during model fitting in the joint space of the two surround cone pooling related parameters,  $V_{\text{narrow}}/V_{\text{wide}}$  and  $R_{\text{narrow}}/R_{\text{wide}}$  for the three examined strategies is depicted by the yellow rectangles. Stars depict the corresponding parameter values in four macaque H1 horizontal cells from the study of Packer & Dacey. **B1-B3** : Line weighting functions of the retinal space referred center and surround cone pooling weights under the three examined strategies. **C1-C3** : vSTF computed under the three strategies are depicted by the gray disks, and the DOG model fit by the gray lines, with the red and blue lines depicting the center and surround components of the DOG model fit. **D1-D3** : Blue and orange bars depict the residuals for the ratios of visual space - referred  $R_s/R_c$  and  $K_s/K_c \times (R_s/R_c)^2$  ratios. Black circles connected by a black line depict the enforced tolerance range in these ratios. The enforced tolerance value in D3 was  $\tau = 0.5$ , and is not visualized. Yellow bars depict the  $\|\mathbf{vSTF}(\omega) - \mathbf{DOG}(\omega)\|$  residual.

2163 **References**

- 2164 [1] Wandell, B.A., Brainard, D.H., Cottaris, N.P.: Visual encoding: Principles and  
2165 software. *Prog Brain Res* **273**(1), 199–229 (2022) <https://doi.org/10.1016/bs.pbr.2022.04.006>
- 2166 [2] Cottaris, N.P., Jiang, H., Ding, X., Wandell, B.A., Brainard, D.H.: A  
2167 computational-observer model of spatial contrast sensitivity: Effects of wave-  
2168 front-based optics, cone-mosaic structure, and inference engine. *J Vis* **19**(4), 8  
2169 (2019) <https://doi.org/10.1167/19.4.8>
- 2170 [3] Cottaris, N.P., Wandell, B.A., Rieke, F., Brainard, D.H.: A computational  
2171 observer model of spatial contrast sensitivity: Effects of photocurrent encod-  
2172 ing, fixational eye movements, and inference engine. *J Vis* **20**(7), 17 (2020)  
2173 <https://doi.org/10.1167/jov.20.7.17>
- 2174 [4] Lian, T., MacKenzie, K.J., Brainard, D.H., Cottaris, N.P., Wandell, B.A.: Ray  
2175 tracing 3d spectral scenes through human optics models. *J Vis* **19**(12), 23 (2019)  
2176 <https://doi.org/10.1167/19.12.23>
- 2177 [5] Nankivil, D., Cottaris, N.P., Brainard, D.H.: Theoretical impact of chromatic  
2178 aberration correction on visual acuity. *Biomed Opt Express* **15**(5), 3265–3284  
2179 (2024) <https://doi.org/10.1364/BOE.516049>
- 2180 [6] Zhang, L.Q., Cottaris, N.P., Brainard, D.H.: An image reconstruction framework  
2181 for characterizing initial visual encoding. *eLife* **11** (2022) <https://doi.org/10.7554/eLife.71132>
- 2182 [7] Kupers, E.R., Carrasco, M., Winawer, J.: Modeling visual performance differences  
2183 'around' the visual field: A computational observer approach. *PLoS Comput Biol*  
2184 **15**(5), 1007063 (2019) <https://doi.org/10.1371/journal.pcbi.1007063>
- 2185 [8] Singh, V., Cottaris, N.P., Heasly, B.S., Brainard, D.H., Burge, J.: Computational  
2186 luminance constancy from naturalistic images. *J Vis* **18**(13), 19 (2018) <https://doi.org/10.1167/18.13.19>
- 2187 [9] Ding, X., Radonjic, A., Cottaris, N.P., Jiang, H., Wandell, B.A., Brainard, D.H.:  
2188 Computational-observer analysis of illumination discrimination. *J Vis* **19**(7), 11  
2189 (2019)
- 2190 [10] Godat, T., Cottaris, N.P., Patterson, S., Kohout, K., Parkins, K., Yang, Q.,  
2191 Strazzeri, J.M., McGregor, J.E., Brainard, D.H., Merigan, W.H., Williams, D.R.:  
2192 In vivo chromatic and spatial tuning of foveolar retinal ganglion cells in macaca  
2193 fascicularis. *PLoS One* **17**(11), 0278261 (2022) <https://doi.org/10.1371/journal.pone.0278261>
- 2194 [11] Osterberg, G., Andersen, H.: Topography of the Layer of Rods and Cones in  
2195 2196 2197 2198 2199 2200 2201 2202 2203 2204 2205 2206 2207 2208

- the Human Retina / by G. Østerberg. A. Busck, Copenhagen (1935). Includes bibliographical references (pages 94-96). 2209  
2210  
2211
- [12] Polyak, S.L.: The Retina; the Anatomy and the Histology of the Retina in Man, Ape, and Monkey, Including the Consideration of Visual Functions, the History of Physiological Optics, and the Histological Laboratory Technique, p. 607. The University of Chicago press, Chicago, Ill., (1941) 2212  
2213  
2214  
2215  
2216
- [13] Dacey, D.M.: The mosaic of midget ganglion cells in the human retina. *J Neurosci* **13**(12), 5334–55 (1993) <https://doi.org/10.1523/JNEUROSCI.13-12-05334.1993> 2217  
2218
- [14] Patterson, S.S., Neitz, M., Neitz, J.: Reconciling color vision models with midget ganglion cell receptive fields. *Front Neurosci* **13**, 865 (2019) <https://doi.org/10.3389/fnins.2019.00865> 2219  
2220  
2221  
2222
- [15] Field, G.D., Gauthier, J.L., Sher, A., Greschner, M., Machado, T.A., Jepson, L.H., Shlens, J., Gunning, D.E., Mathieson, K., Dabrowski, W., Paninski, L., Litke, A.M., Chichilnisky, E.J.: Functional connectivity in the retina at the resolution of photoreceptors. *Nature* **467**(7316), 673–7 (2010) <https://doi.org/10.1038/nature09424> 2223  
2224  
2225  
2226  
2227  
2228
- [16] Wool, L.E., Crook, J.D., Troy, J.B., Packer, O.S., Zaidi, Q., Dacey, D.M.: Non-selective wiring accounts for red-green opponency in midget ganglion cells of the primate retina. *J Neurosci* **38**(6), 1520–1540 (2018) <https://doi.org/10.1523/JNEUROSCI.1688-17.2017> 2229  
2230  
2231  
2232  
2233
- [17] Croner, L.J., Kaplan, E.: Receptive fields of p and m ganglion cells across the primate retina. *Vision Res* **35**(1), 7–24 (1995) [https://doi.org/10.1016/0042-6989\(94\)e0066-t](https://doi.org/10.1016/0042-6989(94)e0066-t) 2234  
2235  
2236  
2237
- [18] Lee, B.B., Shapley, R.M., Hawken, M.J., Sun, H.: Spatial distributions of cone inputs to cells of the parvocellular pathway investigated with cone-isolating gratings. *J Opt Soc Am A Opt Image Sci Vis* **29**(2), 223–32 (2012) <https://doi.org/10.1364/JOSAA.29.00A223> 2238  
2239  
2240  
2241  
2242
- [19] Reid, R.C., Shapley, R.M.: Spatial structure of cone inputs to receptive fields in primate lateral geniculate nucleus. *Nature* **356**(6371), 716–8 (1992) <https://doi.org/10.1038/356716a0> 2243  
2244  
2245  
2246
- [20] Chen, Q., Ingram, N.T., Baudin, J., Angueyra, J.M., Sinha, R., Rieke, F.: Predictably manipulating photoreceptor light responses to reveal their role in downstream visual responses. *eLife* **13** (2024) <https://doi.org/10.7554/eLife.93795> 2247  
2248  
2249  
2250
- [21] Freeman, J., Field, G.D., Li, P.H., Greschner, M., Gunning, D.E., Mathieson, K., Sher, A., Litke, A.M., Paninski, L., Simoncelli, E.P., Chichilnisky, E.J.: Mapping nonlinear receptive field structure in primate retina at single cone resolution. *eLife* 2251  
2252  
2253  
2254

- 2255        4 (2015) <https://doi.org/10.7554/eLife.05241>
- 2256
- 2257 [22] Hong, A., Rieke, F.: On-off asymmetries of nonlinear spatial integration impact  
2258        the encoding of natural stimuli in primate retina. *Investigative Ophthalmology  
2259        Visual Science* **65**(7), 4346–4346 (2024)
- 2260
- 2261 [23] Raghavan, R.T., Kelly, J.G., Hasse, J.M., Levy, P.G., Hawken, M.J., Movshon,  
2262        J.A.: Contrast and luminance gain control in the macaque's lateral geniculate  
2263        nucleus. *eNeuro* **10**(3) (2023) <https://doi.org/10.1523/ENEURO.0515-22.2023>
- 2264 [24] Turner, M.H., Rieke, F.: Synaptic rectification controls nonlinear spatial integra-  
2265        tion of natural visual inputs. *Neuron* **90**(6), 1257–1271 (2016) <https://doi.org/10.1016/j.neuron.2016.05.006>
- 2266
- 2267 [25] Benardete, E.A., Kaplan, E.: The receptive field of the primate p retinal ganglion  
2268        cell, i: Linear dynamics. *Vis Neurosci* **14**(1), 169–85 (1997) <https://doi.org/10.1017/s0952523800008853>
- 2269
- 2270 [26] Croner, L.J., Purpura, K., Kaplan, E.: Response variability in retinal ganglion  
2271        cells of primates. *Proc Natl Acad Sci U S A* **90**(17), 8128–30 (1993) <https://doi.org/10.1073/pnas.90.17.8128>
- 2272
- 2273 [27] Kling, A., Cooler, S., Manookin, M.B., Rhoades, C., Brackbill, N., Field, G.,  
2274        Rieke, F., Sher, A., Litke, A., Chichilnisky, E.J.: Functional diversity in the output  
2275        of the primate retina. *bioRxiv* (2024) <https://doi.org/10.1101/2024.10.31.621339>
- 2276
- 2277 [28] Wohrer, A., Kornprobst, P.: Virtual retina: a biological retina model and sim-  
2278        ulator, with contrast gain control. *J Comput Neurosci* **26**(2), 219–49 (2009)  
2279        <https://doi.org/10.1007/s10827-008-0108-4>
- 2280
- 2281 [29] Ly, K., Italiano, M.L., Shivdasani, M.N., Tsai, D., Zhang, J.Y., Jiang, C., Lovell,  
2282        N.H., Dokos, S., Guo, T.: Virtual human retina: Simulating neural signalling,  
2283        degeneration, and responses to electrical stimulation. *Brain Stimul* **18**(1), 144–163  
2284        (2025) <https://doi.org/10.1016/j.brs.2025.01.013>
- 2285
- 2286 [30] Somaratna, M.A., Freeman, A.W.: The receptive field construction of midget  
2287        ganglion cells in primate retina. *J Neurophysiol* **133**(1), 268–285 (2025) <https://doi.org/10.1152/jn.00302.2024>
- 2288
- 2289 [31] Cottaris, N., Wandell, B., Brainard, D.: Midget retinal ganglion cell surrounds  
2290        in macaque: cone-selective or not? *Journal of Vision* **24**(10), 1090–1090 (2024)  
2291        <https://doi.org/10.1167/jov.24.10.1090>
- 2292
- 2293 [32] Hennig, M.H., Funke, K., Worgotter, F.: The influence of different retinal sub-  
2294        circuits on the nonlinearity of ganglion cell behavior. *J Neurosci* **22**(19), 8726–38  
2295        (2002) <https://doi.org/10.1523/JNEUROSCI.22-19-08726.2002>
- 2296
- 2297
- 2298
- 2299
- 2300

- [33] Pillow, J.W., Paninski, L., Uzzell, V.J., Simoncelli, E.P., Chichilnisky, E.J.: Prediction and decoding of retinal ganglion cell responses with a probabilistic spiking model. *J Neurosci* **25**(47), 11003–13 (2005) <https://doi.org/10.1523/JNEUROSCI.3305-05.2005> 2301  
2302  
2303  
2304  
2305  
2306  
2307  
2308  
2309  
2310  
2311  
2312  
2313  
2314  
2315  
2316  
2317  
2318  
2319  
2320  
2321  
2322  
2323  
2324  
2325  
2326  
2327  
2328  
2329  
2330  
2331  
2332  
2333  
2334  
2335  
2336  
2337  
2338  
2339  
2340  
2341  
2342  
2343  
2344  
2345  
2346
- [34] Watson, A.B.: A formula for human retinal ganglion cell receptive field density as a function of visual field location. *J Vis* **14**(7) (2014) <https://doi.org/10.1167/14.7.15>
- [35] Curcio, C.A., Allen, K.A.: Topography of ganglion cells in human retina. *J Comp Neurol* **300**(1), 5–25 (1990) <https://doi.org/10.1002/cne.903000103>
- [36] Curcio, C.A., Sloan, K.R., Kalina, R.E., Hendrickson, A.E.: Human photoreceptor topography. *J Comp Neurol* **292**(4), 497–523 (1990) <https://doi.org/10.1002/cne.902920402>
- [37] Klug, K., Herr, S., Ngo, I.T., Sterling, P., Schein, S.: Macaque retina contains an s-cone off midget pathway. *J Neurosci* **23**(30), 9881–7 (2003) <https://doi.org/10.1523/JNEUROSCI.23-30-09881.2003>
- [38] Patterson, S.S., Kuchenbecker, J.A., Anderson, J.R., Bordt, A.S., Marshak, D.W., Neitz, M., Neitz, J.: An s-cone circuit for edge detection in the primate retina. *Sci Rep* **9**(1), 11913 (2019) <https://doi.org/10.1038/s41598-019-48042-2>
- [39] Gauthier, J.L., Field, G.D., Sher, A., Shlens, J., Greschner, M., Litke, A.M., Chichilnisky, E.J.: Uniform signal redundancy of parasol and midget ganglion cells in primate retina. *J Neurosci* **29**(14), 4675–80 (2009) <https://doi.org/10.1523/JNEUROSCI.5294-08.2009>
- [40] Kling, A., Gogliettino, A.R., Shah, N.P., Wu, E.G., Brackbill, N., Sher, A., Litke, A.M., Silva, R.A., Chichilnisky, E.J.: Functional organization of midget and parasol ganglion cells in the human retina (2020) <https://doi.org/10.1101/2020.08.07.240762>
- [41] Kolb, H., Marshak, D.: The midget pathways of the primate retina. *Doc Ophthalmol* **106**(1), 67–81 (2003) <https://doi.org/10.1023/a:1022469002511>
- [42] McMahon, M.J., Lankheet, M.J., Lennie, P., Williams, D.R.: Fine structure of parvocellular receptive fields in the primate fovea revealed by laser interferometry. *J Neurosci* **20**(5), 2043–53 (2000) <https://doi.org/10.1523/JNEUROSCI.20-05-02043.2000>
- [43] Packer, O.S., Dacey, D.M.: Receptive field structure of h1 horizontal cells in macaque monkey retina. *J Vis* **2**(4), 272–92 (2002) <https://doi.org/10.1167/2.4.1>
- [44] Smith, V.C., Lee, B.B., Pokorny, J., Martin, P.R., Valberg, A.: Responses

- 2347 of macaque ganglion cells to the relative phase of heterochromatically modu-  
2348 lated lights. *J Physiol* **458**, 191–221 (1992) <https://doi.org/10.1113/jphysiol.1992.sp019413>
- 2349  
2350
- 2351 [45] Polans, J., Jaeken, B., McNabb, R.P., Artal, P., Izatt, J.A.: Wide-field optical  
2352 model of the human eye with asymmetrically tilted and decentered lens that  
2353 reproduces measured ocular aberrations. *Optica* **2**(2), 124–134 (2015) <https://doi.org/10.1364/OPTICA.2.000124>
- 2354  
2355
- 2356 [46] Tuten, W.S., Cooper, R.F., Tiruveedhula, P., Dubra, A., Roorda, A., Cottaris,  
2357 N.P., Brainard, D.H., Morgan, J.I.W.: Spatial summation in the human fovea:  
2358 Do normal optical aberrations and fixational eye movements have an effect? *J Vis*  
2359 **18**(8), 6 (2018) <https://doi.org/10.1167/18.8.6>
- 2360  
2361
- 2362 [47] Schein, S.J.: Anatomy of macaque fovea and spatial densities of neurons in foveal  
2363 representation. *J Comp Neurol* **269**(4), 479–505 (1988) <https://doi.org/10.1002/cne.902690403>
- 2364  
2365
- 2366 [48] Packer, O., Hendrickson, A.E., Curcio, C.A.: Photoreceptor topography of the  
2367 retina in the adult pigtail macaque (macaca nemestrina). *J Comp Neurol* **288**(1),  
2368 165–83 (1989) <https://doi.org/10.1002/cne.902880113>
- 2369  
2370
- 2371 [49] Gogliettino, A.R., Madugula, S.S., Grosberg, L.E., Vilkhu, R.S., Brown, J.,  
2372 Nguyen, H., Kling, A., Hottowy, P., Dabrowski, W., Sher, A., Litke, A.M.,  
2373 Chichilnisky, E.J.: High-fidelity reproduction of visual signals by electrical stim-  
2374 ulation in the central primate retina. *J Neurosci* **43**(25), 4625–4641 (2023)  
2375 <https://doi.org/10.1523/JNEUROSCI.1091-22.2023>
- 2376  
2377
- 2378 [50] Grunert, U., Martin, P.R.: Cell types and cell circuits in human and non-human  
2379 primate retina. *Prog Retin Eye Res*, 100844 (2020) <https://doi.org/10.1016/j.preteyeres.2020.100844>
- 2380  
2381
- 2382 [51] Banks, M.S., Geisler, W.S., Bennett, P.J.: The physical limits of grating visi-  
2383 bility. *Vision Res* **27**(11), 1915–24 (1987) [https://doi.org/10.1016/0042-6989\(87\)90057-5](https://doi.org/10.1016/0042-6989(87)90057-5)
- 2384  
2385
- 2386 [52] Geisler, W.S.: Sequential ideal-observer analysis of visual discriminations. *Psychol  
2387 Rev* **96**(2), 267–314 (1989) <https://doi.org/10.1037/0033-295x.96.2.267>
- 2388  
2389
- 2390 [53] Sekiguchi, N., Williams, D.R., Brainard, D.H.: Efficiency in detection of isolumi-  
2391 nant and isochromatic interference fringes. *J Opt Soc Am A Opt Image Sci Vis*  
2392 **10**(10), 2118–33 (1993) <https://doi.org/10.1364/josaa.10.002118>
- 2393  
2394
- 2395 [54] Casile, A., Victor, J.D., Rucci, M.: Contrast sensitivity reveals an oculomotor  
2396 strategy for temporally encoding space. *Elife* **8** (2019) <https://doi.org/10.7554/eLife.40924>
- 2397  
2398
- 2399  
2400

- [55] Houston, A.J.H., Brainard, D.H., Smithson, H.E., Read, D.J.: Information, movement and adaptation in human vision. bioRxiv, 2025–0905674315 (2025) <https://doi.org/10.1101/2025.09.05.674315> 2393  
2394  
2395  
2396  
2397  
2398  
2399  
2400  
2401  
2402  
2403  
2404  
2405  
2406  
2407  
2408  
2409  
2410  
2411  
2412  
2413  
2414  
2415  
2416  
2417  
2418  
2419  
2420  
2421  
2422  
2423  
2424  
2425  
2426  
2427  
2428  
2429  
2430  
2431  
2432  
2433  
2434  
2435  
2436  
2437  
2438
- [56] Mullen, K.T.: The contrast sensitivity of human colour vision to red-green and blue-yellow chromatic gratings. *J Physiol* **359**, 381–400 (1985) <https://doi.org/10.1113/jphysiol.1985.sp015591> 2393  
2394  
2395  
2396  
2397  
2398  
2399  
2400  
2401  
2402  
2403  
2404  
2405  
2406  
2407  
2408  
2409  
2410  
2411  
2412  
2413  
2414  
2415  
2416  
2417  
2418  
2419  
2420  
2421  
2422  
2423  
2424  
2425  
2426  
2427  
2428  
2429  
2430  
2431  
2432  
2433  
2434  
2435  
2436  
2437  
2438
- [57] Chaparro, A., Stromeier, r. C. F., Huang, E.P., Kronauer, R.E., Eskew, J. R. T.: Colour is what the eye sees best. *Nature* **361**(6410), 348–50 (1993) <https://doi.org/10.1038/361348a0> 2400  
2401  
2402  
2403  
2404  
2405  
2406  
2407  
2408  
2409  
2410  
2411  
2412  
2413  
2414  
2415  
2416  
2417  
2418  
2419  
2420  
2421  
2422  
2423  
2424  
2425  
2426  
2427  
2428  
2429  
2430  
2431  
2432  
2433  
2434  
2435  
2436  
2437  
2438
- [58] Sekiguchi, N., Williams, D.R., Brainard, D.H.: Aberration-free measurements of the visibility of isoluminant gratings. *J Opt Soc Am A Opt Image Sci Vis* **10**(10), 2105–17 (1993) <https://doi.org/10.1364/josaa.10.002105> 2400  
2401  
2402  
2403  
2404  
2405  
2406  
2407  
2408  
2409  
2410  
2411  
2412  
2413  
2414  
2415  
2416  
2417  
2418  
2419  
2420  
2421  
2422  
2423  
2424  
2425  
2426  
2427  
2428  
2429  
2430  
2431  
2432  
2433  
2434  
2435  
2436  
2437  
2438
- [59] Hong, F., Cottaris, N.P., Brainard, D.H.: Limits on human contrast sensitivity imposed by the initial visual encoding. *Journal of Vision* **24**(10), 658–658 (2024) <https://doi.org/10.1167/jov.24.10.658> 2400  
2401  
2402  
2403  
2404  
2405  
2406  
2407  
2408  
2409  
2410  
2411  
2412  
2413  
2414  
2415  
2416  
2417  
2418  
2419  
2420  
2421  
2422  
2423  
2424  
2425  
2426  
2427  
2428  
2429  
2430  
2431  
2432  
2433  
2434  
2435  
2436  
2437  
2438
- [60] Cruz, Y.T., He, J., Eskew, J. Rhea T.: Using s-cone signals to detect the effects of longitudinal chromatic aberration. *Journal of Vision* **19**(15), 6–6 (2019) <https://doi.org/10.1167/19.15.6> 2400  
2401  
2402  
2403  
2404  
2405  
2406  
2407  
2408  
2409  
2410  
2411  
2412  
2413  
2414  
2415  
2416  
2417  
2418  
2419  
2420  
2421  
2422  
2423  
2424  
2425  
2426  
2427  
2428  
2429  
2430  
2431  
2432  
2433  
2434  
2435  
2436  
2437  
2438
- [61] Oh, S., Hong, F., Nankivil, D., Haggerty, E.B., Stauble, R., Cottaris, N.P., Buch, J., Aguirre, G.K., Brainard, D.H.: Variations in human optics explain idiosyncratic patterns in the red-green spatial contrast sensitivity function. *Journal of Vision* **25**(9), 2440–2440 (2025) <https://doi.org/10.1167/jov.25.9.2440> 2400  
2401  
2402  
2403  
2404  
2405  
2406  
2407  
2408  
2409  
2410  
2411  
2412  
2413  
2414  
2415  
2416  
2417  
2418  
2419  
2420  
2421  
2422  
2423  
2424  
2425  
2426  
2427  
2428  
2429  
2430  
2431  
2432  
2433  
2434  
2435  
2436  
2437  
2438
- [62] Hansen, T., Pracejus, L., Gegenfurtner, K.R.: Color perception in the intermediate periphery of the visual field. *J Vis* **9**(4), 26–112 (2009) <https://doi.org/10.1167/9.4.26> 2400  
2401  
2402  
2403  
2404  
2405  
2406  
2407  
2408  
2409  
2410  
2411  
2412  
2413  
2414  
2415  
2416  
2417  
2418  
2419  
2420  
2421  
2422  
2423  
2424  
2425  
2426  
2427  
2428  
2429  
2430  
2431  
2432  
2433  
2434  
2435  
2436  
2437  
2438
- [63] Stockman, A., Brainard, D.H.: In: Bass, M., DeCusatis, C., Enoch, J., Lakshminarayanan, V., Li, G., Macdonald, C., Mahajan, V., Stryland, E. (eds.) *Color vision mechanisms*, pp. 11–111104. McGraw Hill, New York (2010) 2400  
2401  
2402  
2403  
2404  
2405  
2406  
2407  
2408  
2409  
2410  
2411  
2412  
2413  
2414  
2415  
2416  
2417  
2418  
2419  
2420  
2421  
2422  
2423  
2424  
2425  
2426  
2427  
2428  
2429  
2430  
2431  
2432  
2433  
2434  
2435  
2436  
2437  
2438
- [64] Lennie, P., Haake, P.W., Williams, D.R.: In: Landy, M.S., Movshon, J.A. (eds.) *The design of chromatically opponent receptive fields*, pp. 71–82. MIT Press, Cambridge, Mass. (1991). TY - JOUR 2400  
2401  
2402  
2403  
2404  
2405  
2406  
2407  
2408  
2409  
2410  
2411  
2412  
2413  
2414  
2415  
2416  
2417  
2418  
2419  
2420  
2421  
2422  
2423  
2424  
2425  
2426  
2427  
2428  
2429  
2430  
2431  
2432  
2433  
2434  
2435  
2436  
2437  
2438
- [65] Mullen, K.T., Kingdom, F.A.: Losses in peripheral colour sensitivity predicted from "hit and miss" post-receptoral cone connections. *Vision Res* **36**(13), 1995–2000 (1996) [https://doi.org/10.1016/0042-6989\(95\)00261-8](https://doi.org/10.1016/0042-6989(95)00261-8) 2400  
2401  
2402  
2403  
2404  
2405  
2406  
2407  
2408  
2409  
2410  
2411  
2412  
2413  
2414  
2415  
2416  
2417  
2418  
2419  
2420  
2421  
2422  
2423  
2424  
2425  
2426  
2427  
2428  
2429  
2430  
2431  
2432  
2433  
2434  
2435  
2436  
2437  
2438
- [66] Wandell, B.A.: Foundations of Vision. Sinauer, Sunderland, MA (1995) 2400  
2401  
2402  
2403  
2404  
2405  
2406  
2407  
2408  
2409  
2410  
2411  
2412  
2413  
2414  
2415  
2416  
2417  
2418  
2419  
2420  
2421  
2422  
2423  
2424  
2425  
2426  
2427  
2428  
2429  
2430  
2431  
2432  
2433  
2434  
2435  
2436  
2437  
2438

- 2439 [67] Kim, Y.J., Packer, O., Pollreisz, A., Martin, P.R., Grunert, U., Dacey, D.M.:  
2440 Comparative connectomics reveals noncanonical wiring for color vision in human  
2441 foveal retina. *Proc Natl Acad Sci U S A* **120**(18), 2300545120 (2023) <https://doi.org/10.1073/pnas.2300545120>
- 2442
- 2443 [68] Sun, H., Ruttiger, L., Lee, B.B.: The spatiotemporal precision of ganglion cell sig-  
2444 nals: a comparison of physiological and psychophysical performance with moving  
2445 gratings. *Vision Res* **44**(1), 19–33 (2004) <https://doi.org/10.1016/j.visres.2003.08.017>
- 2446
- 2447 [69] Angueyra, J.M., Rieke, F.: Origin and effect of phototransduction noise in primate  
2448 cone photoreceptors. *Nat Neurosci* **16**(11), 1692–700 (2013) <https://doi.org/10.1038/nn.3534>
- 2449
- 2450 [70] Roy, S., Jun, N.Y., Davis, E.L., Pearson, J., Field, G.D.: Inter-mosaic coordination  
2451 of retinal receptive fields. *Nature* **592**(7854), 409–413 (2021) <https://doi.org/10.1038/s41586-021-03317-5>
- 2452
- 2453
- 2454
- 2455
- 2456
- 2457
- 2458
- 2459
- 2460
- 2461
- 2462
- 2463
- 2464
- 2465
- 2466
- 2467
- 2468
- 2469
- 2470
- 2471
- 2472
- 2473
- 2474
- 2475
- 2476
- 2477
- 2478
- 2479
- 2480
- 2481
- 2482
- 2483
- 2484